AGU PUBLICATIONS

JGR

Journal of Geophysical Research: Atmospheres

RESEARCH ARTICLE
10.1002/2016JD026379

Key Points:
- The influencing mechanism of precipitation and skin temperature on root zone soil moisture trend is different in different climate regions
- Increasing precipitation, temperature, and evapotranspiration causes wetting trends in tropical regions while drying trends in arid regions
- Irrigation causes a wetting trend of root zone soil moisture despite decreasing precipitation and rising temperature in temperate regions

Supporting Information:
- Supporting Information S1

Correspondence to:
M. Choi,
mhchoi@skku.edu

Citation:
Zohaib, M., H. Kim, and M. Choi (2017), Evaluating the patterns of spatiotemporal trends of root zone soil moisture in major climate regions in East Asia, *J. Geophys. Res. Atmos.*, *122*, doi:10.1002/2016JD026379.

Received 14 DEC 2016
Accepted 17 JUN 2017
Accepted article online 8 JUL 2017

Evaluating the patterns of spatiotemporal trends of root zone soil moisture in major climate regions in East Asia

Muhammad Zohaib[1], Hyunglok Kim[2], and Minha Choi[1]

[1]Department of Water Resources, Graduate School of Water Resources, Sungkyunkwan University, Suwon, South Korea, [2]School of Earth Ocean and the Environment, University of South Carolina, Columbia, South Carolina, USA

Abstract Root zone soil moisture (RZSM) is a crucial variable in land-atmosphere interactions. Evaluating the spatiotemporal trends and variability patterns of RZSM are essential for discerning the anthropogenic and climate change effects on the regional and global hydrological cycles. In this study, the trends of RZSM, computed by the exponential filter from the European Space Agency's Climate Change Initiative soil moisture, were evaluated in major climate regions of East Asia from 1982 to 2014. Moreover, the trends of RZSM were compared to the trends of precipitation (P), skin temperature (T_{skin}), and actual evapotranspiration (AET) to investigate how they influence the RZSM trends in each climate region. Drying trends were predominant in arid and continental regions, whereas wetting trends were found in the tropical and temperate regions. The increasing trends of T_{skin} and AET cause drying in arid and continental regions, whereas in tropical regions, these cause wetting trends, which might be due to convective P. In temperate regions, despite decreasing P and increasing T_{skin}, the RZSM trend was increasing, attributed to the intensive irrigation activities in these regions. This is probably the first time to analyze the long-term trends of RZSM in different climate regions. Hence, the results of this study will improve our understanding of the regional and global hydrological cycles. Despite certain limitations, the results of this study may be useful for improving and developing climate models and predicting long-term vast scale natural disasters such as drought, dust outbreaks, floods, and heat waves.

1. Introduction

The amount of soil moisture (SM) seems negligible (approximately 0.0012%) compared to the total amount of water in the Earth system [*Gleick*, 1996]. Nevertheless, it is highly important in regulating the water, energy, and carbon fluxes between the land surface and atmosphere [*Koster et al.*, 2004; *Jung et al.*, 2010]. It directs the P between runoff and infiltration, as well as incoming radiation between latent and sensible heat fluxes [*Taylor et al.*, 2012; *Loew et al.*, 2013]. It is also an important parameter for various scientific applications and disaster predictions, which include water resource management, drought predictions, floods, dust outbreaks, and weather predictions [*Dorigo et al.*, 2012; *Loew et al.*, 2013; *Brocca et al.*, 2014a; *Kim and Choi*, 2015; *Kim et al.*, 2017]. In 2010, regarding its importance in hydrological and climate applications, the Global Climate Observation System declared SM as an essential climate variable (ECV) for studying the global climate system [*Dorigo et al.*, 2012, 2015; *Brocca et al.*, 2014b; European Space Agency's Climate Change Initiative, 2010, http://www.esa-soilmoisture-cci.org/].

Studying the trends and variability of SM is of utmost importance for understanding global and regional hydrological cycles. Moreover, it helps in interpreting the effect of human interference and climate change on hydrological processes [*Qiu et al.*, 2016; *Feng*, 2016], which affects weather patterns, water consumption, and agricultural needs. Conventionally, SM variations and its interaction with the climate system have been studied using ground-based observations [*Huang et al.*, 2008; *Guan et al.*, 2009; *Wang et al.*, 2010; *Brocca et al.*, 2011]. However, the limited availability in space and time make their use inappropriate for study at large spatial and temporal scales. Recent studies emphasize the use of model-based SM products to study SM variability and related hydrological variations at larger temporal and spatial extents [*Zhu and Lettenmaier*, 2007; *Yang et al.*, 2007, 2008; *Sheffield and Wood*, 2008]. However, the accuracy of model-based SM highly depends upon several factors, such as the quality of the forcing data sets of a model, the substantial heterogeneity of indistinct soil properties in horizontal and vertical layers, and the nature of the assumptions made for understanding the complex processes [*Ferguson and Wood*, 2011; *Hain et al.*, 2011]. Moreover, most of the currently available land surface models do not incorporate anthropogenic activities, such as irrigation, urbanizations, and large-scale water diversion projects, which significantly change SM dynamics [*Drewniak et al.*, 2013; *Qiu et al.*, 2016; *B. Yang et al.*, 2016].

Remotely based SM retrieval from space is a promising tool for studying the behavior of SM at global and regional scales. Specifically, satellites can view global SM variability through active and passive microwave frequency sensors with sufficient spatial and temporal resolutions and reasonable accuracy [*Entekhabi et al.*, 2010; *Kerr et al.*, 2012; *Wagner et al.*, 2013; *Loew et al.*, 2013]. Many researchers previously used satellite-based SM products, especially from microwave frequency sensors, for examining the spatial and temporal patterns of SM [*Wagner et al.*, 2007; *Juglea et al.*, 2010; *Su et al.*, 2011; *Choi*, 2012; *Rebel et al.*, 2012]. Several global SM products from space have been retrieved with different frequency sensors, retrieval systems, and algorithms [*Njoku et al.*, 2003; *Bartalis et al.*, 2006; *Owe et al.*, 2008], but none of the individual product covers the long-term period needed for climate records and long-term analysis. To obtain long-term SM observations from the space, a first attempt to merge SM products from different active and passive microwave satellites was introduce by *Liu et al.* [2011a, 2012], under the European Space Agency (ESA) Program on Global Monitoring of essential climate variable (ECV). Many studies have utilized the ESA's Climate Change Initiative (CCI) SM for analyzing the SM trend [*Dorigo et al.*, 2012; *Feng and Zhang*, 2015; *Qiu et al.*, 2016; *Chen et al.*, 2016]. Recently, *Feng* [2016] utilized the ESA CCI SM to analyze the isolated effect of climate and vegetation change across different spatial scales. This research found that the climate change is the major contributor to the SM trend globally, whereas vegetation change regulates the SM trend at regional and local scales.

Satellite-based remote sensing provides only near-surface SM (SSM) estimates (0–5 cm); however, RZSM is as important as SSM in land surface-atmosphere interactions because it directs transpiration, which is the largest contributor to total land ET [*Dirmeyer et al.*, 2006; *Lawrence et al.*, 2007; *Seneviratne et al.*, 2010; *Konings and Gentine*, 2016]. The previous researchers showed that RZSM is well correlated with the near-surface SM [*Choi and Jacobs*, 2007; *Albergel et al.*, 2008; *Mahmood et al.*, 2012; *Ford et al.*, 2014]. In this regard, RZSM has been estimated from various satellite surface SM retrievals using the exponential filter method [*Wagner et al.*, 1999], including the European Remote Sensing (ERS) satellite scatterometer [*Wagner et al.*, 1999; *Ceballos et al.*, 2005], advanced scatterometer (ASCAT) [*Albergel et al.*, 2009; *Brocca et al.*, 2010, 2011, 2013], and Soil Moisture and Ocean Salinity (SMOS) [*Ford et al.*, 2014]. The results of validation studies encourage the use of this method for estimating RZSM from surface SM estimates.

This study explores the trend and variability of RZSM in four major climate classes of East Asia (20°N–55°N and 70°E–140°E), according to Köppen climate classes [*Peel et al.*, 2007], for a period of 33 years (1982–2014). The analysis in this study was based on the ESA CCI SM merged product. First, the RZSM was estimated from the ESA CCI SM by the recursive form of the exponential filter [*Albergel et al.*, 2008]. Second, a trend analysis was performed on the time series of RZSM, P, T_{skin}, and AET products in each climate class. Third, the correlation coefficient (R) between RZSM-P and RZSM-T_{skin} was analyzed in each climate class to identify their contribution on the RZSM trend. Finally, the trend pattern in RZSM caused by P and T_{skin} was justified by the trend of AET and the expected influencing mechanism was discussed.

This study is unique because most of the existing literature focuses on the trends of surface SM [*Sheffield and Wood*, 2008; *Dorigo et al.*, 2012; *Cheng et al.*, 2015; *Qiu et al.*, 2016]; however, RZSM is also an essential variable in land-atmosphere interactions. To the best of authors' knowledge, no study has been conducted to analyze the long-term trend and variability of RZSM based on satellite observations in different climate zones. The results of this study will be helpful in improving climate models by considering the trend of RZSM in different climate regions and the effect of human interference on the hydrological cycle.

2. Material and Methodology

2.1. Study Area

The eastern subregion of the Asian continent, East Asia (20°N–55°N, 70°E–140°E), was selected to investigate the RZSM trend in different climate classes. This part of the world is one of the most populous regions with diverse land surface cover and fragile ecosystem and hence is highly vulnerable to climate change [*Shao*, 2004; *Hu et al.*, 2008; *Piao et al.*, 2010; *Liu et al.*, 2015; *Cheng et al.*, 2015].

According to the Köppen-Geiger climate classification, East Asia contains four major climate classes: tropical, arid, temperate, and continental (Figure 1). The tropical climate is dominant in the southern part of the study area, including parts of India, Nepal, Bhutan, and Bangladesh. Annual average P is highly varied, generally

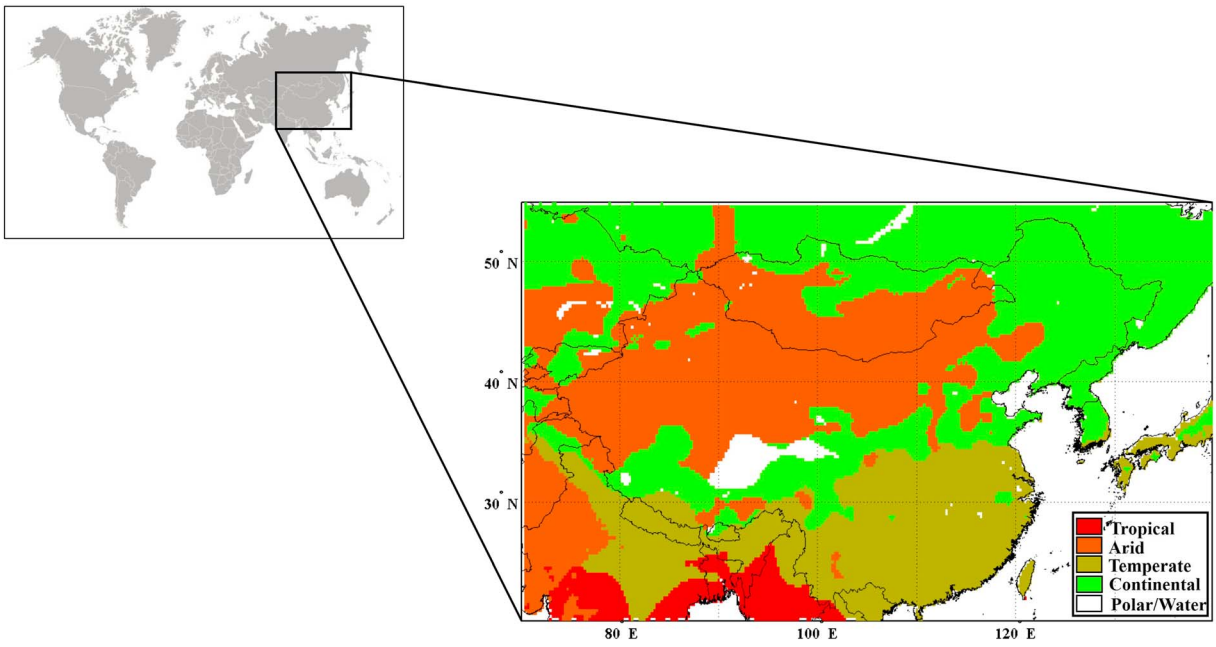

Figure 1. Climate zone classifications of the study region.

above 1000 mm across the region, and reaches up to 2500 mm on the seaside-facing highlands [*Li et al.*, 2012]. Approximately 80% of the *P* falls during the hot-humid season (April–September), and the rest falls during the dry season [*Zhang et al.*, 2006; *Deng et al.*, 2012].

The arid climate is prominent in the high plains and desert regions of northern China and Mongolia and is characterized by large temperature differences between summer and winter [*Li et al.*, 2012]. *P* ranges from 40 to 150 mm yr^{-1} on the plains to 300 mm yr^{-1} in the mountains [*Genxu and Guodong*, 1999].

The temperate climate regions are mostly located in the southeastern regions of China, northern Japan, Nepal, and most part of the India, characterized by mild winters and summers [*Gunaratnam and Li*, 2010]. Mean annual *P* is comparatively low in the north (e.g., approximately 521 mm at Beijing) and somewhat higher in southern China and Japan (1205 mm at Sendai, Japan, and 1683 mm at Guangzhou, China), where it falls mostly in summer as a result of the East Asian Monsoon and typhoons [*Li et al.*, 2012].

The continental climates are characterized by significant annual variation in temperature and are mostly dry; these areas usually occur in the northern hemisphere, because the southern hemisphere mostly consists of the sea. This climate tends to be found between latitudes 37°N and 60°N. In East Asia, this type of climate is found in southern Russia, northeastern China, Siberia, Mongolia, and the Korean Peninsula.

2.2. Data Sets

2.2.1. ESA CCI Soil Moisture

The ESA CCI SM product is an important data set because it is the only long-term satellite-derived SM. The ESA CCI SM data set has a spatial resolution of 0.25° × 0.25° with daily temporal resolution, representing a depth of ~2–5 cm and spanning for a period of 37 years (November 1978 to December 2015). In this study, the latest version 3.2 merged product, released in March 2017, was used. The merged product is derived by blending the active and passive products [*Dorigo et al.*, 2010; *Seneviratne et al.*, 2010; *Liu et al.*, 2011b, 2012]. Active products include the ASCAT onboard the METeorological OPerational (METOP-A and METOP-B) satellite and scatterometers onboard the ERS-1 and ERS-2 satellites. Passive products include the Nimbus 7 scanning multichannel microwave radiometer, the Defense Meteorological Satellite Program Special Sensor Microwave/Imagers, Tropical Rainfall Measuring Mission Microwave Imager, Aqua Advanced Microwave Scanning Radiometer-Earth Observing System, Coriolis WindSat, Global Change Observation Mission 1st-Water Advanced Microwave Scanning Radiometer-2 (AMSR2), and SMOS [*Dorigo et al.*, 2016].

This newer version of ESA CCI data set utilized the improved merging technique based on the signal-to-noise-ratio estimates and the improved estimates of random errors through triple collocation analysis. Before merging the data sets from different sensors, they were harmonized by matching the cumulative density function (CDF) of the absolute SM values to the Global Land Data Assimilation System Noah SM [*Rodell et al.*, 2004]. *Liu et al.* [2012] showed that the CDF matching technique affects the absolute values, but the dynamics and trends are preserved. *Dorigo et al.* [2015] comprehensively validated the ESA CCI SM, using 596 in situ observation sites from 28 different observing networks, and found that its performance varies across the networks and time period. Further, *C. H. Su et al.* [2016] found that the inhomogeneities in the ESA CCI SM data caused by the transition of the sensors, retrieval algorithms, and instrumental drift and failure induce erroneous trends. However, the errors caused by these inhomogeneities were within the acceptable error range of 0.003 $m^3\ m^{-3}\ yr^{-1}$, stated by *Global Climate Observing System* [2011]. Additionally, some previous researchers pointed out the limitations of the microwave-based SM retrievals over extremely dry regions, such as deserts and semideserts [*Gruhier et al.*, 2010; *Wagner et al.*, 2013]. Despite these discrepancies, many researchers previously showed that the trends in the ESA CCI SM are consistent with those from various reanalysis of SM and *P* products as well as vegetation growth [*Albergel et al.*, 2012; *Dorigo et al.*, 2012; *Loew et al.*, 2013]. Based on these previous research studies and improved merging techniques, we expect that the ESA CCI SM data have enough accuracy for predicting RZSM and its trend analysis. Overall, the merged product was supposed to be superior to either active or passive products individually, except regarding the ASCAT product [*Dorigo et al.*, 2015].

2.2.2. ERA-Interim Skin Temperature Data Set

T_{skin}, also known as the radiometric temperature, is derived from thermal emission of the Earth's surface and is generally an average of various canopies and soil surface temperatures [*Hall et al.*, 1992; *Betts et al.*, 1996]. Since it is the physical temperature of the Earth's surface and is more directly related to surface properties than surface-air temperature, it is important for understanding many terrestrial biogeophysical processes [*Prigent et al.*, 2003; *Jin et al.*, 1997]. T_{skin} and air temperature (1.5–2 m) are significantly different in terms of magnitude, response to atmospheric conditions, and diurnal phase [*Garratt*, 1995; *Jin and Dickinson*, 2010]. To derive T_{skin}, the energy and water fluxes at the land-atmosphere interface were parameterized by an updated land surface Hydrology scheme, the Tiles European Centre for Medium-Range Weather Forecasts (ECMWF) Scheme for Surface Exchanges over Land. In this scheme, each grid box is assigned a different set of possible surface types or tiles, namely, bare ground, low and high vegetation, intercepted water, and shaded and exposed snow over land [*Viterbo and Beljaars*, 1995; *Balsamo et al.*, 2009; *Trigo et al.*, 2015]. For each tile, T_{skin} is derived by solving the surface energy balance equation assuming that the skin layer has no heat capacity [*Dutra et al.*, 2010; *Trigo et al.*, 2015]. The ECMWF T_{skin} is then estimated as the weighted average of tiled T_{skin}. *Trigo et al.* [2015] evaluated the ERA-Interim T_{skin}, by the Meteosat Second Generation (MSG) surface temperature, and found that the ERA-Interim T_{skin} slightly overestimates the MSG surface temperature at nighttime and underestimates at daytime, most prominently in arid and semi-arid regions. Similarly, *Fréville et al.* [2014] showed that the ERA-Interim T_{skin} overestimates the Moderate Resolution Imaging Spectroradiometer (MODIS) T_{skin} in Antarctica. Despite this inconsistency in absolute values at the daily time step, it is believed that the ERA-interim T_{skin} is helpful in extracting meaningful information about trends because of its reliable land forcing data, including in situ and satellite observations [*Dee et al.*, 2011]. Various researchers demonstrated the quality of ERA-interim fields by comparing with observation data sets and found good agreement [*Balsamo et al.*, 2009; *Simmons et al.*, 2010; *Szczypta et al.*, 2011; *Decker et al.*, 2012]. The ECMWF ERA-interim reanalysis T_{skin} data set has a spatial resolution of 0.25° × 0.25° and is available from 1979 to 2014. However, in this study, the monthly mean T_{skin} from 1982 to 2014 was used to analyze its effect on RZSM trends.

2.2.3. Multi-Source Weighted-Ensemble Precipitation Data Set

The *P* data from Multi-Source Weighted-Ensemble Precipitation (MSWEP) 3-hourly 0.25° × 0.25° global gridded data set available from 1979 to 2015 [*Beck et al.*, 2016] were used in this study. The data set was designed by merging different *P* data sources of the highest quality available, including gauge-based, satellite, and reanalysis. The long-term mean of MSWEP was based on the Climate Hazards Group Precipitation Climatology data set but was replaced with more accurate regional data sets where available. The gauge undercatch and orographic effect problems were overcome by taking the catchment-averaged *P* from the streamflow (*Q*) across the globe. The temporal variability of MSWEP was determined by weight-averaging

P anomalies from seven different data sets. *Beck et al.* [2016] evaluated the performance of the MSWEP and four other *P* data sets independently against FLUXNET tower stations and for hydrological modeling used in the Hydrologiska Byråns Vattenbalansavdelning hydrological model [*Bergstrôm*, 1992] at 9011 different catchments ($<$50,000 km^2) across the globe. Among all *P* data sets, MSWEP showed the best performance in terms of *R*, Nash-Sutcliffe efficiency (NSE), and root-mean-square error (RMSE) but performed average in terms of absolute bias (median $R = 0.67$ versus 0.44–0.59 and NSE of 0.52 versus 0.29–0.39 for other data sets). *Nair and Indu* [2017] assessed the performance of MSWEP *P* over India in different seasons and found that its performance is region- and season-dependent. However, it showed good performance (*R*: 0.86, bias: −0.049, and RMSE: 0.1788) in detecting daily rainfall and poor performance in detecting the higher extremes with reference to the gauge-based Indian Meteorological Department rainfall.

2.2.4. GLEAM Evapotranspiration Data Set

The Global Land Evaporation Amsterdam Model (GLEAM) is a set of algorithms, specifically developed for estimating the global ET at 0.25° × 0.25° spatial resolution and daily time scale. Also, it provides the RZSM based on a multilayer water-balance model. It is the first global model that utilizes the satellite SM as a forcing data set for constraining potential evaporation rates [*Miralles et al.*, 2011]. This algorithm is mainly based on the *Priestley and Taylor* [1972] radiation-based evaporation model, but it also utilizes the Gash analytical model [*Gash*, 1979; *Miralles et al.*, 2010] to estimate the forest interception loss and vegetation optical depth, a proxy for the vegetation water content [*Liu et al.*, 2013], in the calculation of the evaporative stress [*Miralles et al.*, 2011, 2014b; *Martens et al.*, 2016]. The validation of the third version (v3) GLEAM data set against 64 eddy-covariance towers and 2338 SM sensors across the globe showed an improved performance of SM and ET fluxes in terms of *R* and unbiased root-mean-square difference (ubRMSD): SM (*R*: 0.61 to 0.64 and ubRMSD: 0.060 to 0.059), and ET (*R*: 0.80 to 0.79 and ubRMSD: 0.79 to 0.73). The GLEAM ET and SM data sets have been widely used to study the spatial variability and trends in the water cycle [*Jasechko et al.*, 2013; *Greve et al.*, 2014; *Miralles et al.*, 2014a; *Zhang et al.*, 2016] and land-atmosphere feedback [*Miralles et al.*, 2014b; *Guillod et al.*, 2015]. This study utilizes the AET data set from the third version (v3) of GLEAM [*Martens et al.*, 2016] to inspect its effect on the trends of RZSM in different climate regions of East Asia.

2.2.5. Climate Classification Data Set

The Köppen climate classification system was originally developed by Wladimir *Köppen* [1900] and modified over time by many researchers as more recent data became available [*Triantafyllou and Tsonis*, 1994; *Stern et al.*, 2000]. The Köppen-Geiger climate classification map used in this study is based on a large global data set of long-term monthly *P* and temperature station time series [*Peel et al.*, 2007]. It is available from the Oak Ridge National Laboratory Distributed Active Archive Center (ORNL DAAC) website with an original spatial resolution of 0.1° × 0.1° and resampled to 0.25° × 0.25° by the nearest-neighbor method. We considered four major climate classes—tropical, arid, temperate, and continental—to investigate the RZSM trends and its influencing factors.

3. Methodology

To mask out the water bodies, we used the Noah Land/Sea mask data set, which is based on the MOD44W (MODIS) land/sea mask data set [*Carroll et al.*, 2009].

3.1. Exponential Filter

The exponential filter is a simple two-layer water-balance model proposed by *Wagner et al.* [1999] to relate near-surface SM estimates to profile SM content (details about the method is provided in the supporting information). Many previous studies utilized the exponential filter to estimate RZSM in different regions of the world using various satellite platforms [*Wagner et al.*, 1999; *Albergel et al.*, 2009; *Brocca et al.*, 2010; *Ford et al.*, 2014] and found it a competent method when only surface SM estimates are given. This study utilized the recursive form of the exponential filter [*Albergel et al.*, 2008] for estimating RZSM from the ESA CCI combined product. It is an easy and computationally efficient method to implement [*Ford et al.*, 2014].

$$\mathrm{SWI}_{mn} = \mathrm{SWI}_{m(n-1)} + K_n\left(\mathrm{ms}(t_n)\text{-}\mathrm{SWI}_{m(n-1)}\right) \tag{1}$$

where subscripts m stand for "modeled" and *n* denotes the time step. $\mathrm{SWI}_{m(n-1)}$ is the predicted RZSM estimate at t_{n-1}, $\mathrm{ms}(t_n)$ is the surface SM estimate at t_n, and the gain *K* at time t_n is given by

$$K_n = \frac{K_{n-1}}{K_{n-1} + e^{-\left(\frac{t_n - t_{n-1}}{T}\right)}} \tag{2}$$

where T is the characteristic time length in days and considered as substitute for all the processes that affect the temporal dynamics of SM in the subsurface, such as root zone depth, soil hydraulic properties, evaporation, runoff, and vertical heterogeneity of soil properties [*Albergel et al.*, 2008]. *Wagner et al.* [1999] evaluated the performance of the exponential filter and concluded that any T value between 15 and 30 days gives a satisfactory estimation, even though there may exist T values that perform better. *Albergel et al.* [2008] used an optimized T value (T_{opt}) concept for each site, based on the highest Nash-Sutcliffe score. However, they found that the results of a single T_{opt} for all stations does not make much difference. They further concluded that there is no clear linkage between T_{opt} and soil and climate properties; however, it does depend upon the depth of the root zone. *Ford et al.* [2014] found that under the assumption of homogeneous soil properties throughout the soil column, the exponential filter provides acceptable estimates of RZSM from satellite near-surface SM. Based on the above literature, it can be noted that T value is mostly affected by the depth of root zone, which depends upon the vegetation type [*Y. Yang et al.*, 2016]. However, satellites typically involve in viewing heterogeneous pixels that have different vegetation types in a pixel. Therefore, we used a constant root zone depth of 100 cm, which is commonly used [*Paris Anguela et al.*, 2008; *Reichle et al.*, 2015]. *Wagner et al.* [1999] showed that the best estimates for the layer 0–100 cm can be obtained with $T = 20$ days, which we have chosen in this study. Moreover, it was found that the RZSM obtained by exponential filter does not duplicate the SSM; however, it shows a clear difference in linear trend lines (Figures S1 and S2 in the supporting information).

3.2. Anomaly Calculations

Anomalies were calculated to avoid the seasonal effects that artificially enhance the R between two variables [*Scipal et al.*, 2005, 2008]. The anomaly time series (ANO) was calculated by removing the mean seasonality ($\overline{SM}$) from the original yearly mean time series (ORI), i.e., calculating the overall mean of all the years having 7 months of data (April, May, June, July, August, September, and October), and subtracting it from the original time series of each year. Seasonal anomalies were calculated using the following formula:

$$\overline{SM}_{\text{year}} = \frac{\sum_{YR=1981}^{2014} \text{SM}_{\text{year}}}{N} \tag{3}$$

$$\text{ANO}_{\text{year}} = \text{ORI}_{\text{year}} - \overline{SM}_{\text{year}} \tag{4}$$

3.3. Trend Analysis

Monotonic trends in all the data sets were calculated using the nonparametric Mann-Kendall test [*Kendall*, 1938; *Mann* 1945; *Hirsch and Slack*, 1984]. The null hypothesis (H_0) of the test assumed that there is no significant trend in the examined time series (i.e., the data are independent and randomly ordered). This hypothesis is rejected if the P value of the test statistic is less than the significance level 0.05 [*Dorigo et al.*, 2012; *Albergel et al.*, 2013].

First, the statistical significance of the trends was tested by computing test statistics (S) from all the subsequent data values:

$$S = \sum_{i=1}^{n-1} \sum_{j=i+1}^{n} \text{sgn}\left(x_j - x_i\right) \tag{5}$$

where

$$\text{sgn}\left(x_j - x_i\right) = \begin{cases} +1, \left(x_j - x_i\right) > 0 \\ 0, \left(x_j - x_i\right) = 0 \\ -1, \left(x_j - x_i\right) < 0 \end{cases} \tag{6}$$

$$\text{var}(S) = \frac{1}{18}\left[n(n-1)(2n+5) - \sum_{p=1}^{q} t_p\left(t_p - 1\right)\left(2t_p\right) + 5\right] \tag{7}$$

$$Z = \begin{cases} \dfrac{S-1}{\sqrt{\mathrm{var}(S)}}, & \text{if } S > 0 \\ 0, & \text{if } S = 0 \\ \dfrac{S+1}{\sqrt{\mathrm{var}(S)}}, & \text{if } S < 0 \end{cases} \tag{8}$$

The statistic Z, when compared with the tolerable probability, administers the presence or absence of a statistically significant trend. In this study, a tolerable probability of 0.05 was used.

Besides finding the statistical significance of trend, the slope of the trend was estimated by a simple nonparametric procedure developed by *Sen* [1968]. Sen's slope estimator is the median of the slopes, $Q_{i,j}$, calculated from each pair of x_i and x_j as follows:

$$Q_{i,j} = \frac{x_i - x_j}{t_i - t_j}, t_i > \mathrm{t_j} \tag{9}$$

where x_i and x_j are the measurements at times t_i and t_j. If there are n values of x in the time series, we get as many as $n(n-1)/2$ slope estimates for $Q_{i,j}$ ($t_i > t_j$).

3.4. Correlation Analysis

To quantify the strength and direction of the linear relationship between RZSM-P and RZSM-T_{skin}, the Pearson product-moment R [*Pearson*, 1895] were computed between deseasonalized time series of variables. It is the covariance of the two variables divided by the product of their standard deviations,

$$r = \frac{1}{n-1}\sum_{i=1}^{n}\left(\frac{x_i - \overline{x}}{s_x}\right)\left(\frac{y_i - \overline{y}}{s_y}\right) \tag{10}$$

where x_i and y_i are the ith values and $\overline{x}$,$\overline{y}$, and S_x, S_y are the means and standard deviations of variables x and y, respectively. Significance testing was performed with the two-tailed Student's t test, for which a P value of 0.05 was selected.

4. Results and Discussion

4.1. Data Gaps and Fraction of Spatial Coverage

Previous research has shown that the performance of the ESA CCI SM is not reliable with large data gaps [*Dorigo et al.*, 2015; *Loew et al.*, 2013]. It makes the results of trend analysis erroneous [*Khaliq et al.*, 2009; *Renard et al.*, 2008]. Additionally, few months do not cover all climate zones in East Asia for the entire study period (1982–2014), which will make the analysis biased; thus, we omit the months that have fractional coverage less than 0.7, on average, to enable a reliable comparison of the RZSM trend in each climate region. Moreover, the Tibetan Plateau has missing data in almost all the months except a few; hence, this area was also excluded in the study. The fraction of spatial coverage is determined by calculating the ratio between the number of grid cells reporting a valid value in each month and the number of grid cells that reported a valid value in the month of maximum coverage during the entire period [*McNally et al.*, 2016]. Figure 2 shows the boxplots of spatial fraction coverage of the available data on a monthly time scale for 1982–2014 over East Asia. It is observed that the spatial coverage in January, February, March, November, and December has many missing data even at monthly time scale, with a median value less than 0.7. However, the rest of the months have spatial fraction coverage greater than 0.7, approximating 0.9. Based on this outcome, further analysis in this study was carried out only for the months of April to October.

Moreover, the reliability of the ESA CCI RZSM (0–100 cm) in different climate classes was evaluated by comparing them with the average SM of the 0–100 cm layer from ERA-Interim at a monthly time scale. On average, R values are 0.471, 0.707, 0.259, and 0.497 in the tropical, arid, temperate, and continental climate regions, respectively. Biases are, on average, 0.0289 m^3m^3, 0.0585 m^3m^3, 0.0193 m^3m^3, and 0.0655 m^3m^3; RMSE values, on average, are 0.0256 m^3m^3, 0.0214 m^3m^3, 0.0210 m^3m^3, and 0.0193 m^3m^3, respectively (Table S1 in the supporting information).

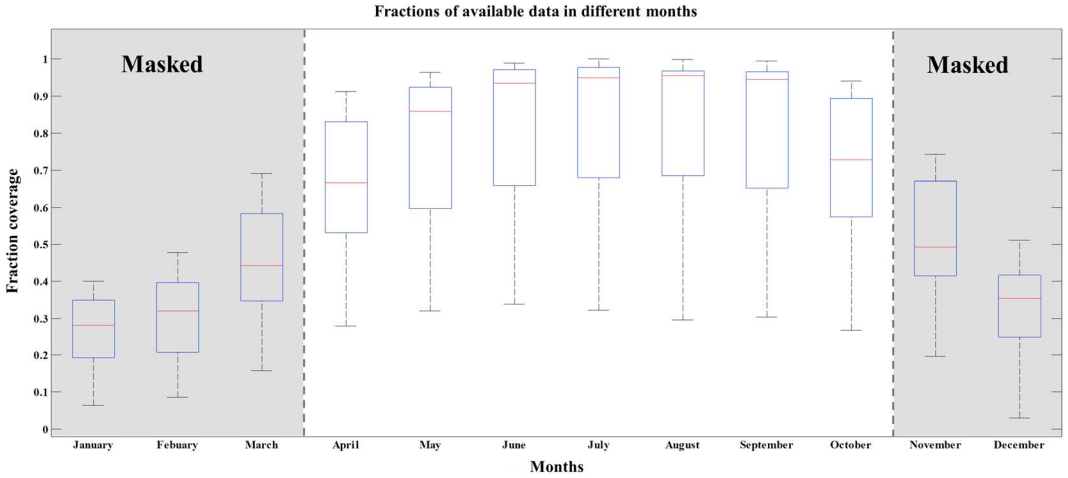

Figure 2. ESA CCI SM monthly data coverage over East Asia in different months of 1982–2014.

4.2. Changes in Skin Temperature and Precipitation Trends

Figure 3 shows the time series, calculated by taking the spatial mean, of T_{skin} for the four major climate classes in East Asia. From 1982 to 2014, the average annual T_{skin} significantly increases in East Asia at the 0.05 α level. Here we divided the entire study period into two halves, 1982–2000 and 2001–2014, to evaluate the temporal variations of RZSM, AET, T_{skin}, and P. Generally, a change in the sign of the T_{skin} trend can be seen in the tropical and arid regions. In tropical regions, the trend is downward in the first half of the study period but upward in the second half (Figure 3a), whereas in arid regions, upward in the first half and downward in the second half of the study period (Figure 3b). The pattern of the T_{skin} trend in both temperate and continental climates are increasing in both halves of the study periods (Figures 3c and 3d). However, in the continental climate regions, T_{skin} increases with a steep slope in the first half and increases with a mild slope in the second half of the study period (Figure 3d). Moreover, in Figure 3, the annual fluctuations in T_{skin} anomalies in all climatic subregions are very high. Additionally, it is worth noting that the anomalies of T_{skin} in arid, temperate, and continental regions are negative in the first half of the study period and positive in the second half, which infers that under the global warming, T_{skin} is rising in recent years.

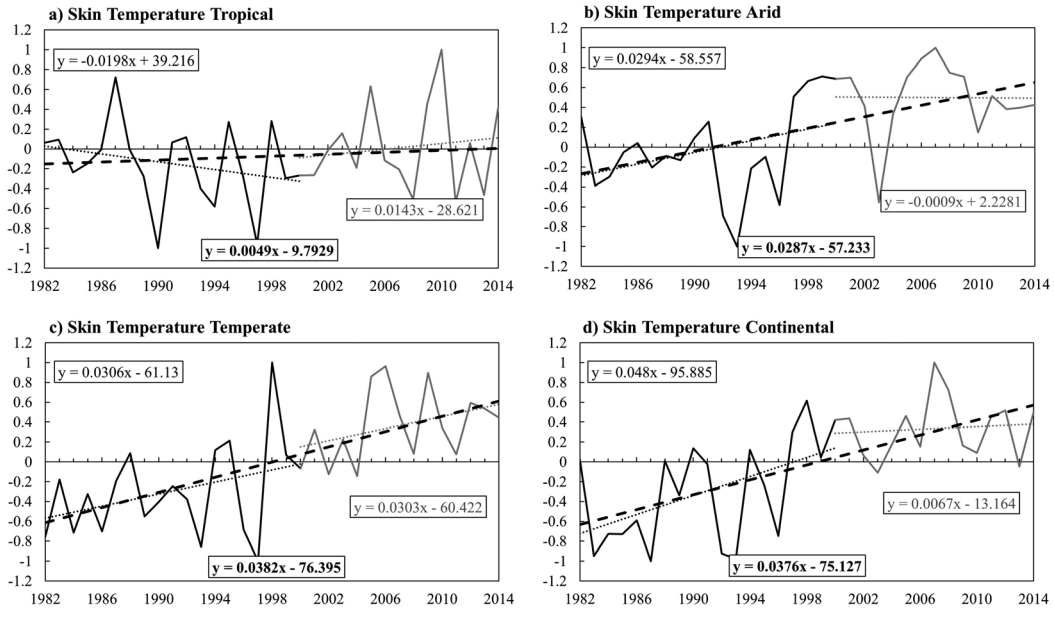

Figure 3. Anomaly time series of skin temperature for 1982–2014 in different climate class of East Asia (a) tropical, (b) arid, (c) temperate, and (d) continental.

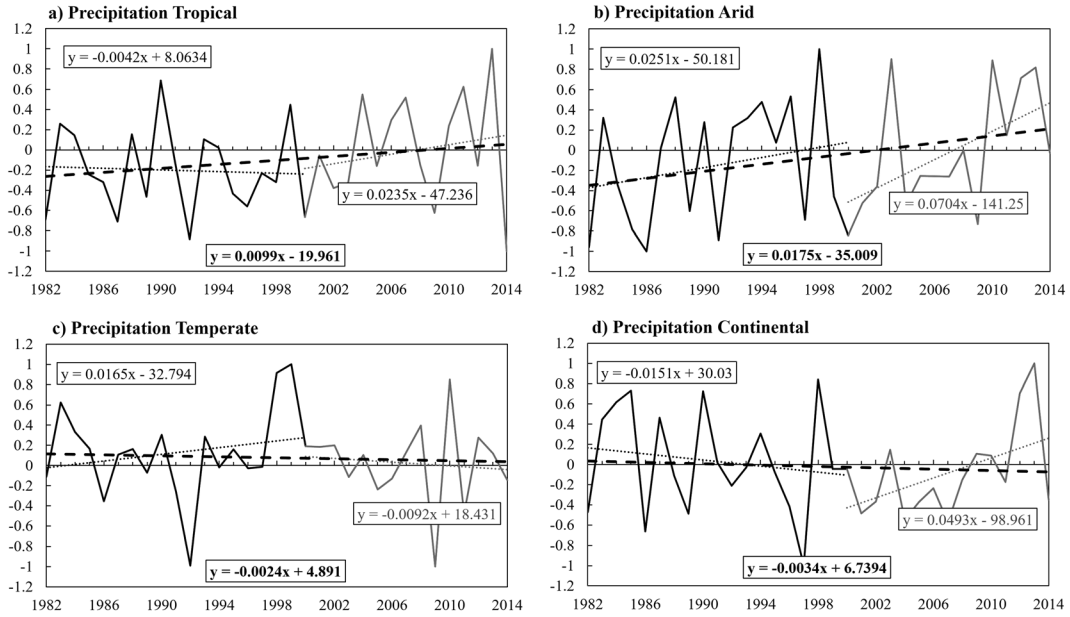

Figure 4. Anomaly time series of precipitation for 1982–2014 in different climate class of East Asia (a) tropical, (b) arid, (c) temperate, and (d) continental.

Similarly, Figure 4 shows the anomaly time series of spatially integrated *P* for the four major climate classes in East Asia. Generally, annual *P* increases in East Asia for 1982–2014, but this is not significant at the 0.05 α level. Specifically, in both the tropical and continental climate regions of East Asia, *P* decreases in the first half of study period, whereas it increases in the second half. The overall trend in tropical regions is increasing, whereas it is decreasing in continental regions (Figures 4a and 4d). In arid climate regions, *P* increases throughout the study period. Finally, in temperate climate regions, overall, a decreasing trend of *P* can be seen, despite increases in the first half of the study period and decreases in the second half of the study period. Less rainfall in temperate climate regions and high annual rainfall in tropical climate regions align with the Intergovernmental Panel on Climate Change report [*Intergovernmental Panel on Climate Change*, 2007]. Moreover, Figure 4 also shows high annual fluctuations of *P* anomalies in all subregions.

4.3. Spatial Pattern of Trends and Correlations of *P*, T_{skin}, RZSM, and AET in East Asia

R values were employed to detect linkages of *P*, AET, and T_{skin} with the RZSM in different climate regions. Generally, the *R* of RZSM is positive with *P* and negative with T_{skin} in all climate classes (Figure 5), except for temperate regions, where both *P* and T_{skin} have a weak positive *R* with RZSM (Table 1).

Figure 6 shows the spatial distribution of the linear trends of yearly mean *P* (mm yr^{-1}), T_{skin} (K yr^{-1}), RZSM (m^3 m^{-3} yr^{-1}), and AET (mm yr^{-1}) for 1982–2014. Table 2 shows that 53% of the land area in East Asia has a drying trend and 47% has a wetting trend of RZSM (Figure 6a), however, 36% of the total trends were found significant at the 0.05 α level. The most prominent drying is found in southern Russia near Lake Baikal, eastern Kazakhstan, southwestern Mongolia, and the West Bengal and Bihar districts of India. The drying over these regions is consistent with the warming trend of the T_{skin} (Figure 6c). In general, the results of our study are consistent with previous literature [*Dorigo et al.*, 2012; *Greve et al.*, 2014; *Cheng et al.*, 2015] that found significant drying trends for SM over East Asia. Conversely, notable wetting trends can be seen in central and southern China, central and northeast India, and northern Mongolia. The wetting trend in central China might be ascribed by the heavy irrigation application in these regions. Toward the south, Jianxi, Hubei, and Hunan provinces have major irrigated fields, whereas in the north, the Huang-Huai-Hai plain is located, which is the most intensively irrigated region of the world [*Siebert et al.*, 2005; *Shi et al.*, 2014; *Qiu et al.*, 2016; *B. Yang et al.*, 2016]. This finding is also verified by comparing the trends of the ESA CCI RZSM with the ERA-interim RZSM, which does not include irrigation modules, and shows increasing and decreasing

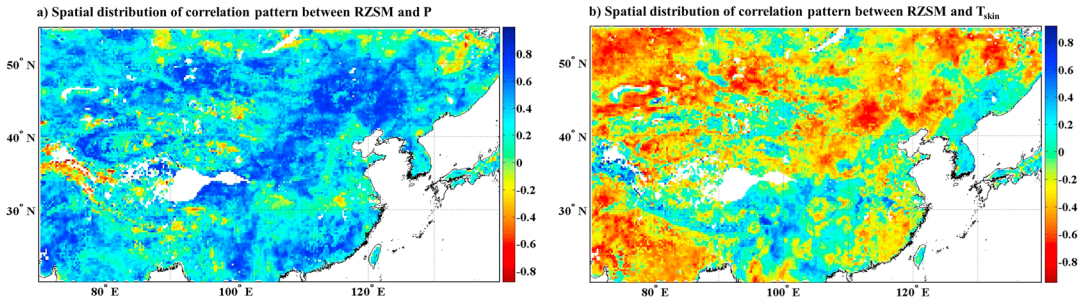

Figure 5. Pixel wise spatial distribution of correlation coefficient for 33 year (1982–2014) mean values between (a) RZSM-*P* and (b) RZSM-T_{skin}.

trends, respectively (Figure S3). Hence, it can be assumed that human attempts to improve crop production could significantly affect the regional- to global-scale climate conditions not only in short-term but also in long-term periods.

Figure 6b shows the spatial distribution of the MSWEP *P* trend over East Asia. Overall, 55% of the pixels showed increasing trends and 15% of the total trends are significant at 0.05 α level (Table 2). Generally, *P* shows an increasing trend in the arid regions of China, Korean Peninsula, coastal region of northern China and India, and East Kazakhstan. Conversely, a drying trend can be observed in the central Mongolia, northern China extending to Russian Far East. Similar spatial trend patterns in East Asia was also found by *Kim and Park* [2016]. However, a notable decreasing trend was found over the northeastern states of India: Assam, Meghalaya, and Nagaland. A potential reason for the drying trend of *P* in these regions can be related to the long-term warming of the tropical oceans, which possibly decrease the land-sea thermal gradient and the amount of moisture transported from the Bay of Bengal [*Roxy et al.*, 2015; *Tan et al.*, 2016; *Latif et al.*, 2016]. These northeastern states of India are in the temperate climate regions, where the primary mode of *P* is frontal depressions. These frontal depression phenomena are diminished due to the lessened moisture transport from the Bay of Bengal, Indian Ocean. The decrease in *P* over northeast India is also consistent with the previous literature [*Deka et al.*, 2013; *Das et al.*, 2014; *Mishra and Liu*, 2014].

Figure 6c shows the spatial distribution of the ERA-Interim T_{skin} trend over East Asia. Overall, 97% of the pixels showed an increasing trend and 60% of the total trends are significant at 0.05 α level (Table 2). The most prominent warming trend is found north of 40°N and in the central China. The warming trend over the northern part of the East Asia is consistent with the previous literature [*Huang et al.*, 2014; *Ji et al.*, 2014; *Cheng et al.*, 2015]. The increase in temperature may be primarily caused by the high rate of greenhouse gases produced over the mainland of East Asia [*Tett et al.*, 1999; *Kang et al.*, 2015]. This perception can be supported by the results of studies concluding that China is one of the world's largest contributor to the greenhouse gases [*Piao et al.*, 2010; *Kan*, 2011] having a concentration of 10,975.50 $MtCO_2e$ for the year 2012 (Climate Analysis Indicators Tool (CAIT) Version 2.0, World Resources Institute (Washington, DC: World Resources Institute, 2014), Retrieved 2014–06–27, http://cait.wri.org/).

The GLEAM AET shows an overall increasing trend in 72% of the pixels, while 37% of the total trends were significant, out of which 86% was increasing (Table 2). The most prominent increasing trend of ET was found on the southern coast of China and in the deserts of Kazakhstan and Rajasthan, India (Figure 6d). The increasing trend of ET in these regions may be caused by the increasing trend of T_{skin} except in some arid regions of China, where an afforestation program was initiated by the Chinese government for environmental restoration [*Wang et al.*, 2007; *Cao et al.*, 2011]. Conversely, the most notable decreasing trend was found in most of Mongolia, northern China, and Burma, which may be attributed to the decreasing trend of *P* in these areas.

Table 1. Summary of Correlation Coefficient in Different Climate Classes

	Tropical	Arid	Temperate	Continental
RZSM-*P*	0.432	0.541	0.201	0.304
RZSM-T_{skin}	−0.372	−0.591	0.204	−0.330

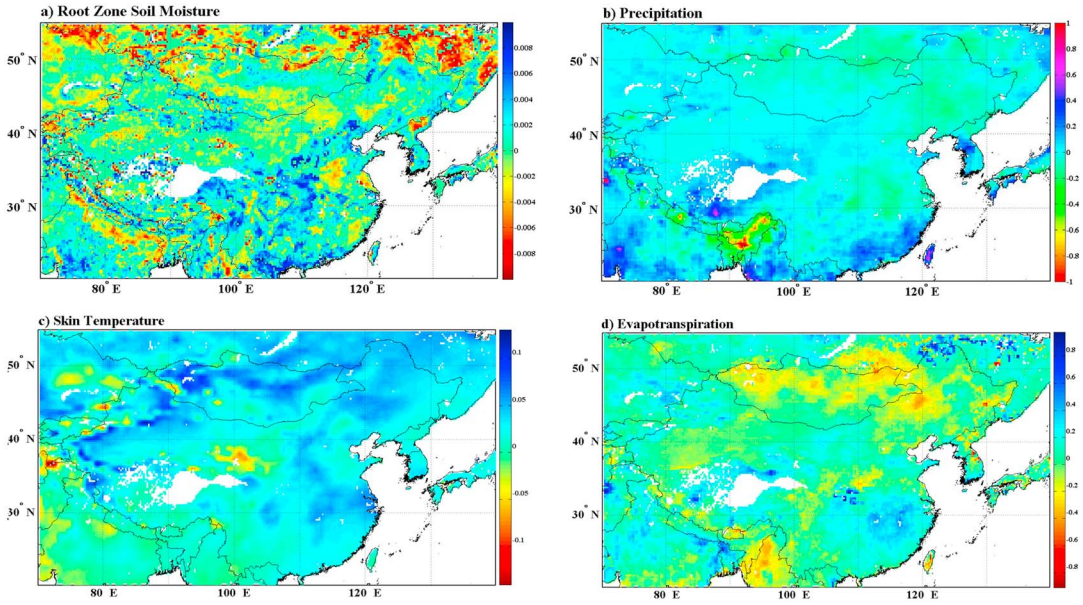

Figure 6. The spatial distribution of linear trend for mean (a) root zone soil moisture, (b) precipitation, (c) skin temperature, and (d) evapotranspiration from 1982 to 2014 (the white color shows ocean and Tibetan Plateau).

4.4. Integrated Effect of Hydrothermal Conditions on RZSM Trends in Different Climate Class

Overall, a decreasing trend of the RZSM was found in East Asia, which is not significant at an α level of 0.05 but is significant at the 0.1. Moreover, an insignificant increasing trend of P and a significant increasing trend of T_{skin} and ET were found in East Asia.

Figure 7 shows the anomaly time series of RZSM in different climate classes. Figure 7a shows that in the tropical climate regions of East Asia, RZSM has a significant increasing trend. Moreover, high interannual variability can also be observed, with 1987 as the driest year and 1999 and 2001 as the wettest years. Tropical regions are characterized by hot average temperatures all year round, dense vegetation, and high monthly P, typically not less than 60 mm a month, with annual P greater than 2000 mm. The increasing trend of RZSM is accompanied by increasing trends of T_{skin} (Figure 3a), P (Figure 4a), and AET (Figure 8a). The increasing trend of RZSM and AET in humid and densely vegetated regions are consistent with the finding of *Feng* [2016], who ascribed this by the fact that vegetation increases the holding capacity of water and infiltration, hence reducing the draining of water by the runoff. Moreover, significant positive R between RZSM and P is supplemented by the significant negative R between RZSM and T_{skin}. These patterns of trends and R values can be explained by the convective P in tropical regions, initiated primarily by the regional SM [*Guillod et al.*, 2015; *Taylor*, 2015], where an increase in P is associated with a warming climate that strengthens the hydrological cycle [*Held and Soden*, 2006]. Furthermore, previous researchers also found a similar relationship in tropical climate regions, stating the "warmer-gets-wetter" paradigm [*Chadwick et al.*, 2013; *Huang et al.*, 2013, *Tan et al.*, 2015].

In the arid regions of East Asia, the anomaly time series of RZSM (Figure 7b) shows an insignificant decreasing trend at the 0.05 α level. Specifically, a sign change of the linear trend line can be seen in the two halves of the

Table 2. Summary of the Pixel-Wise Distribution of Total and Significant, Positive, and Negative Trends of RZSM, P, T_{skin}, and AET

	Total Trends		Significant Trends		
	Positive	Negative	% of Total	Positive	Negative
RZSM	47	53	36	44	56
P	55	45	15	68	32
T_{skin}	97	3	61	97	3
AET	72	28	37	86	14

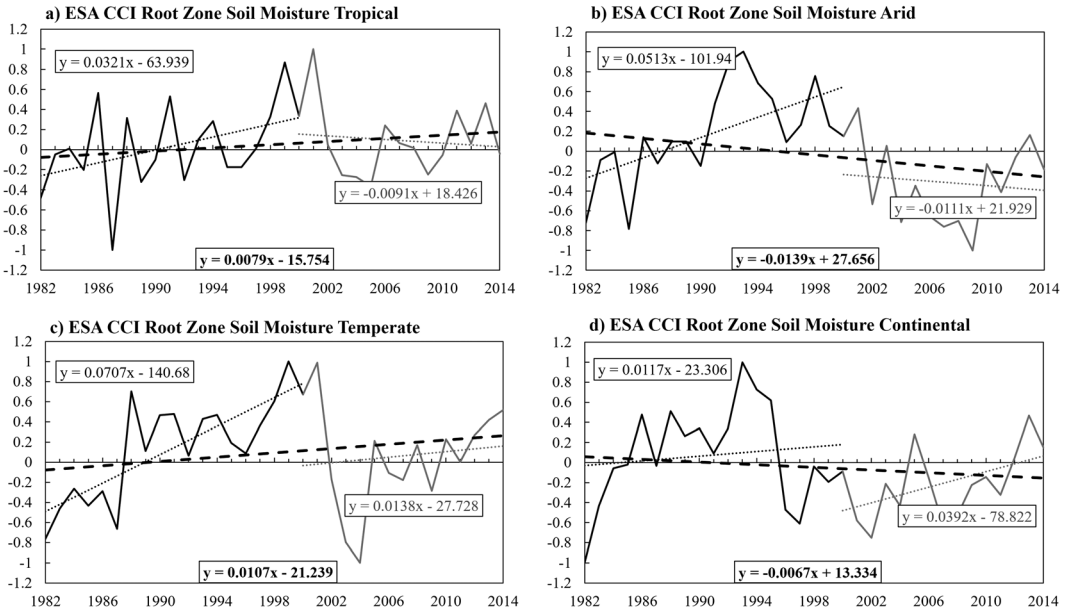

Figure 7. Anomaly time series of root zone soil moisture for 1982–2014 in different climate class of East Asia (a) tropical, (b) arid, (c) temperate, and (d) continental.

study period. However, the overall linear trend is decreasing for the whole study period, which might be caused by the negative anomalies in 2002–2010, a relatively drier period. Both P and T_{skin} strongly correlate with RZSM in the arid regions (Figure 5) and have increasing trends (Figures 3b and 4b). The increasing trend of P and decreasing trend of RZSM are accompanied by the increasing trend of T_{skin} (Figure 3b) and AET (Figure 8b) over the arid regions. This decreasing pattern of RZSM despite increasing P might be explained by the concentrated rainfall during the summer season, almost 80% in May–September, when the soil is comparatively drier [*Chen et al.*, 2006]. The high temperatures over arid regions cause surface water to evaporate prior to infiltrating into the root zone [*Small et al.*, 1999; *Pal et al.*, 2000]. The other potential reason

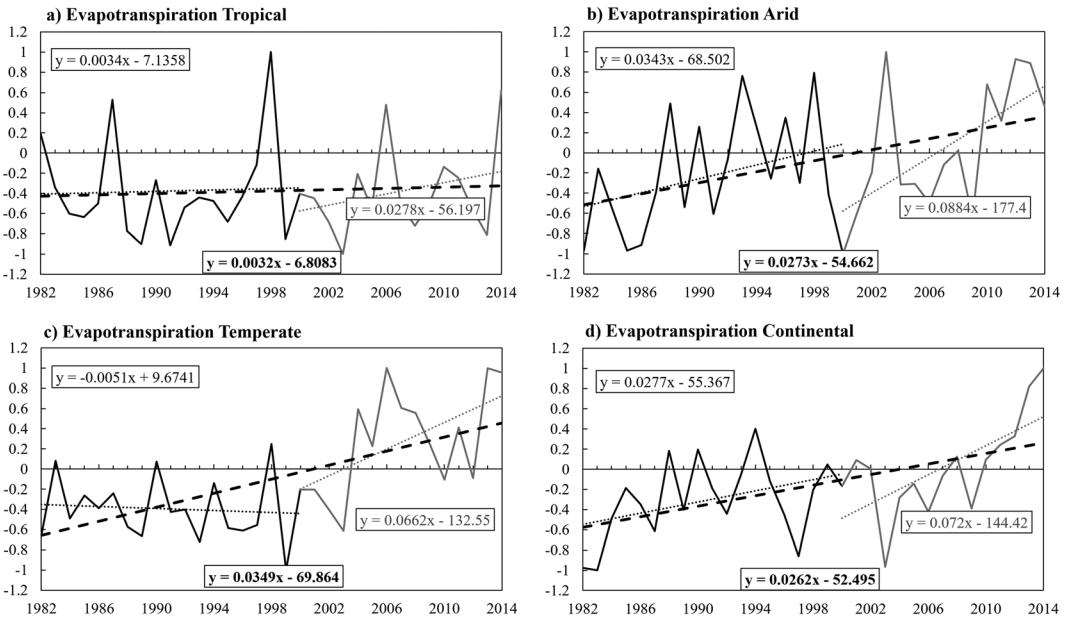

Figure 8. Anomaly time series of evapotranspiration for 1982–2014 in different climate class of East Asia (a) tropical, (b) arid, (c) temperate, and (d) continental.

Table 3. Summary of Trend Patterns of Hydrometeorological Variables: P, T_{skin}, RZSM, and AET, in Different Climate Regions

	P	T_{skin}	RZSM	AET
Tropical	Increasing(0.092) (not significant)	Increasing(0.0021) (not significant)	Increasing(0.00083) (significant)	Increasing(0.010) (not significant)
Arid	Increasing(0.010) (not significant)	Increasing(0.0255) (significant)	Decreasing(−0.00005) (not significant)	Increasing(0.0496) (not significant)
Temperate	Decreasing(−0.0587) (not significant)	Increasing(0.0148) (significant)	Increasing(0.00090) (significant)	Increasing(0.1182) (significant)
Continental	Decreasing(−0.0046) (not significant)	Increasing(0.0296) (significant)	Decreasing(−0.00041) (significant)	Increasing(0.0673) (significant)
East Asia	Increasing(0.00089) (not significant)	Increasing(0.0217) (significant)	Decreasing(−0.00057) (significant at 0.1)	Increasing(0.0824) (significant)

might be the fast drainage of P because arid and dry regions mostly comprise sandy soil and cracks in the soil that allow P to bypass the root zone quickly [*Hillel*, 1998; *Seneviratne et al.*, 2010; *Liu et al.*, 2010]. Moreover, SM does not depend only on P but rather mostly on the surface water balance of P, AET, and runoff [*B. Su et al.*, 2016]. Hence, the afforestation practice under the "ecology restoration program" in the water-limited, arid areas of China may also cause a decreasing trend of the RZSM by encouraging the ET and, thus, causing drying of the soils [*Cao et al.*, 2011]. Similarly, *Feng* [2016] also demonstrated that increase in vegetation in arid and low vegetation area can aggravate the drying of soil. Further, *McColl et al.* [2017] figured out that the low RZSM in the arid regions is not only dependent upon P but is also caused by the greater portioning of the water cycle by the SSM storage.

In the temperate climate regions of East Asia, the RZSM anomaly time series (Figure 7c) shows a significant increasing trend at the 0.05 α level. A high interannual variability can be observed along a sign change of the linear trend in both halves of the study period. Moreover, the linear R of RZSM with P (0.201) and T_{skin} (0.204) are both weak and positive (Table 1). Interestingly, RZSM is increasing, although P (Figure 4c) is decreasing, and T_{skin} (Figure 3c) and AET (Figure 8c) are increasing in the temperate regions. This climate region mostly comprises of the southern and central China, which are the most intensively irrigated areas that might have cause this abnormal pattern of the R and RZSM trend. Irrigation reduces soil albedo, increases soil heat capacity, alters local SM content, and affects the water/energy budget by transforming the ET regime from SM-limited to energy-limited.

In the continental climate regions of East Asia, the RZSM anomaly time series (Figure 7d) shows a significant decreasing trend at the 0.05 α level. Despite the increasing trend of RZSM in both halves of the study period, the overall trend is decreasing because the anomalies are mostly negative in the second half. Moreover, the R of RZSM is positive with P (0.304) and negative with T_{skin} (−0.330). These results suggest that the trend of RZSM in continental regions depends on both T_{skin} and P. The decreasing trend of the RZSM is consistent with the decreasing trend of P and increasing trend of T_{skin}. This finding is further supplemented by the increasing trend of AET in the continental regions (Figure 8d). *Liu et al*. [2016] also found an increasing trend of AET in northern China due to the increase in vegetation greenness by the forest plantations for environmental restoration [*Wang et al.*, 2007; *Cao et al.*, 2011]. The forest plantation projects of China in water-limited areas have a negative impact on environmental restoration [*Cao et al.*, 2011]. Generally, it was found that RZSM, P, T_{skin}, and AET all have different signs and magnitudes of trends in each climate region (Table 3).

5. Conclusions

In this study, we analyzed the spatiotemporal trend and variability of RZSM, as derived from the satellite-based SSM retrievals provided by the ESA CCI, in East Asia for 1982–2014. Moreover, we also compared the RZSM trend with the trends of three hydrometeorological variables—P, T_{skin}, and AET—in different climate classes to investigate the major influencing factors in each climate region. Generally, RZSM has a decreasing trend accompanied by a slightly increasing trend of P and a sharply increasing trend of AET and T_{skin} in East Asia (Table 3). However, the intriguing results are that the direction and magnitude of the trends are heterogeneous across different climate regions. Moreover, the influencing factors such as P and T_{skin} have different effects on the trend of RZSM in each climate region. Specifically, in the tropical climate regions, the trend of RZSM is increasing along with increasing trends of P, T_{skin}, and AET, substantiating the intensified

hydrological cycle and the paradigm "warmer gets wetter" [*Taylor*, 2015; *Feng and Zhang*, 2015]. Interestingly, in arid climate regions, RZSM trend decreases despite increasing *P*. Potential reasons might be the rapid loss of surface water by instant evaporation due to high temperature and the quick drainage of rainfall through sandy soils or cracks in arid regions [*Hillel*, 1998; *Seneviratne et al.*, 2010; *Liu et al.*, 2010]. In temperate climate regions, RZSM increases regardless of decreasing *P* and increasing AET and T_{skin}. This abnormal relationship among RZSM, *P*, and T_{skin} was thought to be induced by the human interference to the hydrological cycle by intensive irrigation. In regions with a continental climate, decreasing RZSM trend was triggered by the decreasing *P* and increasing T_{skin} along with increasing trend of AET. This could be ascribed by the afforestation in water-limited regions of northern China under global warming. The findings of this study might be important in developing and improving climate models to study the dynamics of climate systems and predicting natural disasters, such as agricultural drought, dust, and landslides. The ESA CCI SM merged product (v3.2) used in this study is an improved version because the individual products were merged based on a relatively modern technique, the weighted signal-to-noise-ratio. However, in future, a better understanding of the physical processes, by the field surveys, will improve the retrieval algorithms of satellite and the parameterization of the model data sets; hence, more reliable results could be expected. Moreover, in future, incorporation of the most recently launched missions such as Sentinel-1 and 2, and Soil Moisture Active Passive's level-4 SM, yielding RZSM data sets, into the ESA CCI merged SM product will give us novel insights into the investigation of long-term RZSM trends at a global scale.

Acknowledgments
This research was supported by the Space Core Technology Program through the National Research Foundation of Korea (NRF), funded by the Ministry of Science, ICT and Future Planning (2014M1A3A3A03067387). This work was also supported by the National Research Foundation of Korea (NRF) grant funded by the Korea government (MSIP) (NRF-2016R1A2B4008312). We are thankful to the availability of the ESA CCI SM data from ESA website, T_{skin} and ERA-Interim SM form ECMWF website, MSWEP precipitation data from www.gloh2o.org website, AET data from GLEAM websites, and Köppen-Geiger climate classification data from ORNL DAAC website. Besides, we appreciate the efforts of two anonymous reviewers whose suggestions helped to improve and clarify the manuscript.

References

Albergel, C., C. Rüdiger, T. Pellarin, J. C. Calvet, N. Fritz, F. Froissard, D. Suquia, A. Petitpa, B. Piguet, and E. Martin (2008), From near-surface to root-zone soil moisture using an exponential filter: An assessment of the method based on in-situ observations and model simulations, *Hydrol. Earth Syst. Sci. Discuss.*, *12*, 1323–1337, doi:10.5194/hess-12-1323-2008.

Albergel, C., C. Rüdiger, D. Carrer, J. C. Calvet, N. Fritz, V. Naeimi, Z. Bartalis, and S. Hasenauer (2009), An evaluation of ASCAT surface soil moisture products with in-situ observations in southwestern France, *Hydrol. Earth Syst. Sci.*, *13*(2), 115–124, doi:10.5194/hess-13-115-2009.

Albergel, C., P. de Rosnay, C. Gruhier, J. Muñoz-Sabater, S. Hasenauer, L. Isaksen, Y. Kerr, and W. Wagner (2012), Evaluation of remotely sensed and modeled soil moisture products using global ground-based in situ observations, *Remote Sens. Environ.*, *118*, 215–226, doi:10.1016/j.rse.2011.11.017.

Albergel, C., W. Dorigo, R. H. Reichle, G. Balsamo, P. de Rosnay, J. Muñoz-Sabater, L. Isaksen, R. de Jeu, and W. Wagner (2013), Skill and global trend analysis of soil moisture from reanalyses and microwave remote sensing, *J. Hydrometeorol.*, *14*(4), 1259–1277, doi:10.1175/JHM-D-12-0161.1.

Balsamo, G., P. Viterbo, A. Beljaars, B. van den Hurk, A. K. Betts, and K. Scipal (2009), A revised hydrology for the ECMWF model: Verification from field site to terrestrial water storage and impact in the Integrated Forecast System, *J. Hydrometeorol.*, *10*, 623–643, doi:10.1175/2008JHM1068.1171.

Bartalis, Z., K. Scipal, and W. Wagner (2006), Azimuthal anisotropy of scatterometer measurements over land, *IEEE Trans. Geosci. Remote Sens.*, *44*(8), 2083–2092, doi:10.1109/TGRS.2006.872084.

Beck, H. E., A. I. van Dijk, V. Levizzani, J. Schellekens, D. G. Miralles, B. Martens, and A. de Roo (2016), MSWEP: 3-hourly 0.25° global gridded precipitation (1979–2015) by merging gauge, satellite, and reanalysis data, *Hydrol. Earth Syst. Sci. Discuss.*, 1–38, doi:10.5194/hess-2016-236.

Bergstrôm, S. (1992), The HBV model—Its structure and applications, SMH1 Reports Hydrology No. 4, Swedish Meteorological and hydrological Institute, S-60176 Norrkoping, Sweden.

Betts, A. K., J. H. Ball, A. Beljaars, M. J. Miller, and P. A. Viterbo (1996), The land surface-atmosphere interaction: A review based on observational and global modeling perspectives, *J. Geophys. Res.*, *101*, 7209–7225, doi:10.1029/95JD02135.

Brocca, L., F. Melone, T. Moramarco, W. Wagner, V. Naeimi, Z. Bartalis, and S. Hasenauer (2010), Improving runoff prediction through the assimilation of the ASCAT soil moisture product, *Hydrol. Earth Syst. Sci.*, *14*(10), 1881–1893, doi:10.5194/hess-14-1881-2010.

Brocca, L., et al. (2011), Soil moisture estimation through ASCAT and AMSR-E sensors: An intercomparison and validation study across Europe, *Remote Sens. Environ.*, *115*(12), 3390–3408, doi:10.1016/j.rse.2011.08.003.

Brocca, L., F. Melone, T. Moramarco, and W. Wagner (2013), A new method for rainfall estimation through soil moisture observations, *Geophys. Res. Lett.*, *40*, 853–858, doi:10.1002/grl.50173.

Brocca, L., L. Ciabatta, C. Massari, T. Moramarco, S. Hahn, S. Hasenauer, R. Kidd, W. Dorigo, W. Wagner, and V. Levizzani (2014a), Soil as a natural rain gauge: Estimating global rainfall from satellite soil moisture data, *J. Geophys. Res. Atmos.*, *119*, 5128–5141, doi:10.1002/2014JD021489.

Brocca, L., S. Camici, F. Melone, T. Moramarco, J. Martínez-Fernández, J. F. Didon-Lescot, and R. Morbidelli (2014b), Improving the representation of soil moisture by using a semi-analytical infiltration model, *Hydrol. Process.*, *28*(4), 2103–2115, doi:10.1002/hyp.9766.

Cao, S., L. Chen, D. Shankman, C. Wang, X. Wang, and H. Zhang (2011), Excessive reliance on afforestation in China's arid and semi-arid regions: Lessons in ecological restoration, *Earth Sci. Rev.*, *104*(4), 240–245, doi:10.1016/j.earscirev.2010.11.002.

Carroll, M. L., J. R. Townshend, C. M. DiMiceli, P. Noojipady, and R. A. Sohlberg (2009), A new global raster water mask at 250 m resolution, *Int. J. Digit. Earth*, *2*(4), 291–308, doi:10.1080/17538940902951401.

Ceballos, A., K. Scipal, W. Wagner, and J. Martínez-Fernández (2005), Validation of ERS scatterometer-derived soil moisture data in the central part of the Duero Basin, Spain, *Hydrol. Process.*, *19*(8), 1549–1566, doi:10.1002/hyp.5585.

Chadwick, R., I. Boutle, and G. Martin (2013), Spatial patterns of precipitation change in CMIP5: Why the rich do not get richer in the tropics, *J. Clim.*, *26*(11), 3803–3822, doi:10.1175/JCLI-D-12-00543.1.

Chen, X., Y. Su, J. Liao, J. Shang, T. Dong, C. Wang, W. Liu, G. Zhou, and L. Liu (2016), Detecting significant decreasing trends of land surface soil moisture in eastern China during the past three decades (1979–2010), *J. Geophys. Res. Atmos.*, *121*, 5177–5192, doi:10.1002/2015JD024676.

Chen, Y., K. Takeuchi, C. Xu, Y. Chen, and Z. Xu (2006), Regional climate change and its effects on river runoff in the Tarim Basin, China, *Hydrol. Process.*, *20*(10), 2207–2216, doi:10.1002/hyp.6200.
Cheng, S., X. Guan, J. Huang, F. Ji, and R. Guo (2015), Long-term trend and variability of soil moisture over East Asia, *J. Geophys. Res. Atmos.*, *120*, 8658–8670, doi:10.1002/2015JD023206.
Choi, M. (2012), Evaluation of multiple surface soil moisture for Korean regional flux monitoring network sites: Advanced Microwave Scanning Radiometer E, land surface model, and ground measurements, *Hydrol. Process.*, *26*(4), 597–603, doi:10.1002/hyp.8160.
Choi, M., and J. M. Jacobs (2007), Soil moisture variability of root zone profiles within SMEX02 remote sensing footprints, *Adv. Water Resour.*, *30*(4), 883–896, doi:10.1016/j.advwatres.2006.07.007.
Decker, M., M. A. Brunke, Z. Wang, K. Sakaguchi, X. Zeng, and M. G. Bosilovich (2012), Evaluation of the reanalysis products from GSFC, NCEP, and ECMWF using flux tower observations, *J. Clim.*, *25*(6), 1916–1944, doi:10.1175/JCLI-D-11-00004.1.
Das, P. K., A. Chakraborty, and M. V. R. Seshasai (2014), Spatial analysis of temporal trend of rainfall and rainy days during the Indian Summer Monsoon season using daily gridded (0.5 × 0.5) rainfall data for the period of 1971–2005, *Meteorol. Appl.*, *21*(3), 481–493, doi:10.1002/met.1361.
Dee, D. P., et al. (2011), The ERA-Interim reanalysis: Configuration and performance of the data assimilation system, *Q. J. R. Meteorol. Soc.*, *137*(656), 553–597, doi:10.1002/qj.828.
Deka, R. L., C. Mahanta, H. Pathak, K. K. Nath, and S. Das (2013), Trends and fluctuations of rainfall regime in the Brahmaputra and Barak basins of Assam, India, *Theor. Appl. Climatol.*, *114*(1–2), 61–71, doi:10.1007/s00704-012-0820-x.
Deng, Q., D. Hui, D. Zhang, G. Zhou, J. Liu, S. Liu, G. Chu, and J. Li (2012), Effects of precipitation increase on soil respiration: A three-year field experiment in subtropical forests in China, *PLoS One*, *7*(7), e41493, doi:10.1371/journal.pone.0041493.
Dirmeyer, P. A., X. Gao, M. Zhao, Z. Guo, T. Oki, and N. Hanasaki (2006), GSWP-2: Multimodel analysis and implications for our perception of the land surface, *Bull. Am. Meteorol. Soc.*, *87*(10), 1381–1397, doi:10.1175/BAMS-87-10-1381.
Dorigo, W., R. Jeu, D. Chung, R. Parinussa, Y. Liu, W. Wagner, and D. Fernández-Prieto (2012), Evaluating global trends (1988–2010) in harmonized multi-satellite surface soil moisture, *Geophys. Res. Lett.*, *39*, L18405, doi:10.1029/2012GL052988.
Dorigo, W. A., K. Scipal, R. M. Parinussa, Y. Y. Liu, W. Wagner, R. A. de Jeu, and V. Naeimi (2010), Error characterisation of global active and passive microwave soil moisture datasets, *Hydrol. Earth Syst. Sci.*, *14*(12), 2605–2616, doi:10.5194/hess-14-2605-2010.
Dorigo, W. A., et al. (2015), Evaluation of the ESA CCI soil moisture product using ground-based observations, *Remote Sens. Environ.*, *162*, 380–395, doi:10.1016/j.rse.2014.07.023.
Dorigo, W. A., et al. (2016), Soil moisture [in "State of the climate in 2015"], *Bull. Am. Meteorol. Soc.*, *97*(8), S31–S32.
Drewniak, B., J. Song, J. Prell, V. R. Kotamarthi, and R. Jacob (2013), Modeling agriculture in the community land model, *Geosci. Model Dev.*, *6*(2), 495–515, doi:10.5194/gmd-6-495-2013.
Dutra, E., G. Balsamo, P. Viterbo, P. M. Miranda, A. Beljaars, C. Schär, and K. Elder (2010), An improved snow scheme for the ECMWF land surface model: Description and offline validation, *J. Hydrometeorol.*, *11*(4), 899–916, doi:10.1175/2010JHM1249.1.
Entekhabi, D., et al. (2010), The soil moisture active passive (SMAP) mission, *Proc. IEEE*, *98*(5), 704–716, doi:10.1109/JPROC.2010.2043918.
Feng, H. (2016), Individual contributions of climate and vegetation change to soil moisture trends across multiple spatial scales, *Sci. Rep.*, *6*, doi:10.1038/srep32782.
Feng, H., and M. Zhang (2015), Global land moisture trends: Drier in dry and wetter in wet over land, *Sci. Rep.*, *5*, 18,018, doi:10.1038/srep18018.
Ferguson, C. R., and E. F. Wood (2011), Observed land-atmosphere coupling from satellite remote sensing and reanalysis, *J. Hydrometeorol.*, *12*(6), 1221–1254, doi:10.1175/2011JHM1380.1.
Ford, T. W., E. Harris, and S. M. Quiring (2014), Estimating root zone soil moisture using near-surface observations from SMOS, *Hydrol. Earth Syst. Sci.*, *18*(1), 139–154, doi:10.5194/hess-18-139-2014.
Fréville, H., E. Brun, G. Picard, N. Tatarinova, L. Arnaud, C. Lanconelli, C. Reijmer, and M. van den Broeke (2014), Using MODIS land surface temperatures and the Crocus snow model to understand the warm bias of ERA-Interim reanalyses at the surface in Antarctica, *Cryosphere*, *8*(4), 1361–1373, doi:10.5194/tc-8-1361-2014.
Garratt, J. R. (1995), Observed screen (air) and GCM surface/screen temperatures: Implications for outgoing longwave fluxes at the surface, *J. Clim.*, *8*(5), 1360–1368, doi:10.1175/1520-0442(1995)008<1360:OSAGST>2.0.CO;2.
Gash, J. H. C. (1979), An analytical model of rainfall interception by forests, *Q. J. R. Meteorol. Soc.*, *105*(443), 43–55, doi:10.1002/qj.49710544304.
Genxu, W., and C. Guodong (1999), Water resource development and its influence on the environment in arid areas of China—The case of the Hei River basin, *J. Arid Environ.*, *43*(2), 121–131, doi:10.1006/jare.1999.0563.
Gleick, P. H. (1996), Water resources, in *Encyclopedia of Climate and Weather*, vol. 2, edited by S. H. Schneider, pp. 817–823, Oxford Univ. Press, New York.
Global Climate Observing System (2011), Systematic observation requirements for satellite-based data products for climate: The supplemental details to the satellite-based component of the "Implementation plan for the global observing system for climate in support of the UNFCCC (2010 update, GCOS-154)". [Available at https://www.wmo.int/pages/prog/gcos/documents/SatelliteSupplement2011Update.pdf.]
Greve, P., B. Orlowsky, B. Mueller, J. Sheffield, M. Reichstein, and S. I. Seneviratne (2014), Global assessment of trends in wetting and drying over land, *Nat. Geosci.*, *7*(10), 716–721, doi:10.1038/ngeo2247.
Gruhier, C., et al. (2010), Soil moisture active and passive microwave products: Intercomparison and evaluation over a Sahelian site, *Hydrol. Earth Syst. Sci.*, *14*(1), 141–156, doi:10.5194/hess-14-141-2010.
Guan, X., J. Huang, N. Guo, J. Bi, and G. Wang (2009), Variability of soil moisture and its relationship with surface albedo and soil thermal parameters over the Loess Plateau, *Adv. Atmos. Sci.*, *26*, 692–700, doi:10.1007/s00376-009-8198-0.
Guillod, B. P., B. Orlowsky, D. G. Miralles, A. J. Teuling, and S. I. Seneviratne (2015), Reconciling spatial and temporal soil moisture effects on afternoon rainfall, *Nat. Commun.*, *6*, doi:10.1038/ncomms7443.
Gunaratnam, D., and Z. Li (2010), Strengthening of water resources management in Guiyang: IWRM towards demand management, Asian Development Bank.
Hain, C. R., W. T. Crow, J. R. Mecikalski, M. C. Anderson, and T. Holmes (2011), An intercomparison of available soil moisture estimates from thermal infrared and passive microwave remote sensing and land surface modeling, *J. Geophys. Res.*, *116*, D15107, doi:10.1029/2011JD015633.
Hall, F. G., K. F. Huemmrich, S. J. Goetz, P. J. Sellers, and J. E. Nickeson (1992), Satellite remote sensing of surface energy balance: Success, failures, and unresolved issues in FIFE, *J. Geophys. Res.*, *97*, 19,061–19,089, doi:10.1029/92JD02189.
Held, I. M., and B. J. Soden (2006), Robust responses of the hydrological cycle to global warming, *J. Clim.*, *19*(21), 5686–5699, doi:10.1175/JCLI3990.1.

Hillel, D. (1998), *Environmental Soil Physics*, p. 771, Academic Press, San Diego, Calif.
Hirsch, R. M., and J. R. Slack (1984), A nonparametric trend test for seasonal data with serial dependence, *Water Resour. Res.*, *20*, 727–732, doi:10.1029/WR020i006p00727.
Hu, D., S. L. Huang, Q. Feng, F. Li, J. J. Zhao, Y. H. Zhao, and B. N. Wang (2008), Relationships between rapid urban development and the appropriation of ecosystems in Jiangyin City, Eastern China, *Landsc. Urban Plan.*, *87*(3), 180–191, doi:10.1016/j.landurbplan.2008.06.001.
Huang, J., et al. (2008), An overview of the semi-arid climate and environment research observatory over the Loess Plateau, *Adv. Atmos. Sci.*, *25*, 906–921, doi:10.1007/s00376-008-0906-7.
Huang, J., T. Wang, W. Wang, Z. Li, and H. Yan (2014), Climate effects of dust aerosols over East Asian arid and semiarid regions, *J. Geophys. Res. Atmos.*, *119*, 11,398–11,416, doi:10.1002/2014JD021796.
Huang, P., S. P. Xie, K. Hu, G. Huang, and R. Huang (2013), Patterns of the seasonal response of tropical rainfall to global warming, *Nat. Geosci.*, *6*(5), 357–361, doi:10.1038/ngeo1792.
Intergovernmental Panel on Climate Change (2007), *IPCC Fourth Assessment Report: Climate Change 2007*, p. 472, Cambridge Univ. Press, Cambridge.
Jasechko, S., Z. D. Sharp, J. J. Gibson, S. J. Birks, Y. Yi, and P. J. Fawcett (2013), Terrestrial water fluxes dominated by transpiration, *Nature*, *496*(7445), 347–350, doi:10.1038/nature11983.
Ji, F., Z. Wu, J. Huang, and E. P. Chassignet (2014), Evolution of land surface air temperature trend, *Nat. Clim. Chang.*, *4*(6), 462–466, doi:10.1038/nclimate2223.
Jin, M., and R. E. Dickinson (2010), Land surface skin temperature climatology: Benefitting from the strengths of satellite observations, *Environ. Res. Lett.*, *5*(4), 1–13.
Jin, M., R. E. Dickinson, and A. M. Vogelmann (1997), A comparison of CCM2-BATS skin temperature and surface-air temperature with satellite and surface observations, *J. Clim.*, *10*(7), 1505–1524, doi:10.1175/1520-0442(1997)010<1505:ACOCBS>2.0.CO;2.
Juglea, S., Y. H. Kerr, A. Mialon, J. P. Wigneron, E. Lopez-Baeza, A. Cano, A. Albitar, C. Millan-Scheiding, M. Carmen Antolin, and S. Delwart (2010), Modelling soil moisture at SMOS scale by use of a SVAT model over the Valencia Anchor Station, *Hydrol. Earth Syst. Sci.*, *14*, 831–846, doi:10.5194/hess-14-831-2010.
Jung, M., et al. (2010), Recent decline in the global land evapotranspiration trend due to limited moisture supply, *Nature*, *467*(7318), 951–954, doi:10.1038/nature09396.
Kan, H. (2011), Climate change and human health in China, *Environ. Health Prespect.*, *119*(2), A60–A61, doi:10.1289/ehp.1003354.
Kang, S. M., R. Seager, D. M. Frierson, and X. Liu (2015), Croll revisited: Why is the northern hemisphere warmer than the southern hemisphere?, *Clim. Dyn.*, *44*(5–6), 1457–1472, doi:10.1007/s00382-014-2147-z.
Kendall, M. G. (1938), A new measure of rank correlation, *Biometrika*, *30*(1/2), 81–93, doi:10.2307/2332226.
Kerr, Y. H., et al. (2012), The SMOS soil moisture retrieval algorithm, *IEEE Trans. Geosci. Remote Sens.*, *50*(5), 1384–1403, doi:10.1109/TGRS.2012.2184548.
Khaliq, M. N., T. B. Ouarda, P. Gachon, L. Sushama, and A. St-Hilaire (2009), Identification of hydrological trends in the presence of serial and cross correlations: A review of selected methods and their application to annual flow regimes of Canadian rivers, *J. Hydrol.*, *368*(1), 117–130, doi:10.1016/j.jhydrol.2009.01.035.
Kim, H., and M. Choi (2015), Impact of soil moisture on dust outbreaks in East Asia: Using satellite and assimilation data, *Geophys. Res. Lett.*, *42*, 2789–2796, doi:10.1002/2015GL063325.
Kim, J., and S. K. Park (2016), Uncertainties in calculating precipitation climatology in East Asia, *Hydrol. Earth Syst. Sci.*, *20*(2), 651–658, doi:10.5194/hess-20-651-2016.
Kim, H., M. Zohaib, E. Cho, Y. H. Kerr, and M. Choi (2017), Development and assessment of the sand dust prediction model by utilizing microwave-based satellite soil moisture and reanalysis datasets in East Asian desert areas, *Adv. Meteorol.*, 2017, doi:10.1155/2017/1917372.
Konings, A. G., and P. Gentine (2016), Global variations in ecosystem-scale isohydricity, *Global Change Biol.*, doi:10.1111/gcb.13389.
Köppen, W. (1900), Attempt to classify the climates, preferably according to their relations to the plant world, *Geogr. J.*, *6*(11 H), 593–611. [Available at http://www.jstor.org/stable/27803924.]
Koster, R. D., et al. (2004), Regions of strong coupling between soil moisture and precipitation, *Science*, *305*(5687), 1138–1140, doi:10.1126/science.1100217.
Latif, M., F. S. Syed, and A. Hannachi (2016), Rainfall trends in the South Asian summer monsoon and its related large-scale dynamics with focus over Pakistan, *Clim. Dyn.*, 1–17, doi:10.1007/s00382-016-3284-3.
Lawrence, D. M., P. E. Thornton, K. W. Oleson, and G. B. Bonan (2007), The partitioning of evapotranspiration into transpiration, soil evaporation, and canopy evaporation in a GCM: Impacts on land-atmosphere interaction, *J. Hydrometeorol.*, *8*(4), 862–880, doi:10.1175/JHM596.1.
Li, X., G. Turner, and L. Jiang (2012), Grow in concert with nature: Sustaining East Asia's water resources management through green water defense, World Bank Publ., doi:10.1596/978-0-8213-9588-2.
Liu, Y., et al. (2015), Agriculture intensifies soil moisture decline in Northern China, *Sci. Rep.*, *5*, doi:10.1038/srep11261.
Liu, Y., J. Xiao, W. Ju, K. Xu, Y. Zhou, and Y. Zhao (2016), Recent trends in vegetation greenness in China significantly altered annual evapotranspiration and water yield, *Environ. Res. Lett.*, *11*(9), 094010, doi:10.1088/1748-9326/11/9/094010.
Liu, Y. Y., J. P. Evans, M. F. McCabe, R. A. de Jeu, A. I. J. M. van Dijk, and H. Su (2010), Influence of cracking clays on satellite estimated and model simulated soil moisture, *Hydrol. Earth Syst. Sci.*, *14*(6), 979, doi:10.5194/hess-14-979-2010.
Liu, Y. Y., R. A. de Jeu, M. F. McCabe, J. P. Evans, and A. I. van Dijk (2011a), Global long-term passive microwave satellite-based retrievals of vegetation optical depth, *Geophys. Res. Lett.*, *38*, L18402, doi:10.1029/2011GL048684.
Liu, Y. Y., R. M. Parinussa, W. A. Dorigo, R. A. De Jeu, W. Wagner, A. I. J. M. van Dijk, M. F. McCabe, and J. P. Evans (2011b), Developing an improved soil moisture dataset by blending passive and active microwave satellite-based retrievals, *Hydrol. Earth Syst. Sci.*, *15*(2), 425–436, doi:10.5194/hess-15-425-2011.
Liu, Y. Y., W. A. Dorigo, R. M. Parinussa, R. A. de Jeu, W. Wagner, M. F. McCabe, J. Evans, and A. I. J. M. van Dijk (2012), Trend-preserving blending of passive and active microwave soil moisture retrievals, *Remote Sens. Environ.*, *123*, 280–297, doi:10.1016/j.rse.2012.03.014.
Liu, Y. Y., A. I. Dijk, M. F. McCabe, J. P. Evans, and R. A. Jeu (2013), Global vegetation biomass change (1988–2008) and attribution to environmental and human drivers, *Glob. Ecol. Biogeogr.*, *22*(6), 692–705, doi:10.1111/geb.12024.
Loew, A., T. Stacke, W. Dorigo, R. D. Jeu, and S. Hagemann (2013), Potential and limitations of multidecadal satellite soil moisture observations for selected climate model evaluation studies, *Hydrol. Earth Syst. Sci.*, *17*(9), 3523–3542, doi:10.5194/hess-17-3523-2013.
Mahmood, R., A. Littell, K. G. Hubbard, and J. You (2012), Observed data-based assessment of relationships among soil moisture at various depths, precipitation, and temperature, *Appl. Geogr.*, *34*, 255–264, doi:10.1016/j.apgeog.2011.11.009.
Mann, H. B. (1945), Nonparametric tests against trend. Econometrica, *J. Econometric Soc.*, 245–259, doi:10.2307/1907187.

Martens, B., D. Miralles, H. Lievens, D. Fernández-Prieto, and N. E. C. Verhoest (2016), Improving terrestrial evaporation estimates over continental Australia through assimilation of SMOS soil moisture, *Int. J. Appl. Earth Obs. Geoinf.*, *48*, 146–162, doi:10.1016/j.jag.2015.09.012.
McColl, K. A., S. H. Alemohammad, R. Akbar, A. G. Konings, S. Yueh, and D. Entekhabi (2017), The global distribution and dynamics of surface soil moisture, *Nat. Geosci.*, *10*(2), 100–104, doi:10.1038/ngeo2868.
McNally, A., S. Shukla, K. R. Arsenault, S. Wang, C. D. Peters-Lidard, and J. P. Verdin (2016), Evaluating ESA CCI soil moisture in East Africa, *Int. J. Appl. Earth Obs. Geoinf.*, *48*, 96–109, doi:10.1016/j.jag.2016.01.001.
Miralles, D. G., J. H. Gash, T. R. Holmes, R. A. de Jeu, and A. J. Dolman (2010), Global canopy interception from satellite observations, *J. Geophys. Res.*, *115*, D16122, doi:10.1029/2009JD013530.
Miralles, D. G., T. R. H. Holmes, R. A. M. De Jeu, J. H. Gash, A. G. C. A. Meesters, and A. J. Dolman (2011), Global land-surface evaporation estimated from satellite-based observations, *Hydrol. Earth Syst. Sci.*, *15*(2), 453–469, doi:10.5194/hess-15-453-2011.
Miralles, D. G., A. J. Teuling, C. C. van Heerwaarden, and J. V. G. de Arellano (2014a), Mega-heatwave temperatures due to combined soil desiccation and atmospheric heat accumulation, *Nat. Geosci.*, *7*(5), 345–349, doi:10.1038/ngeo2141.
Miralles, D. G., et al. (2014b), El Niño–la Niña cycle and recent trends in continental evaporation, *Nat. Clim. Chang.*, *4*(2), 122–126, doi:10.1038/nclimate2068.
Mishra, A., and S. C. Liu (2014), Changes in precipitation pattern and risk of drought over India in the context of global warming, *J. Geophys. Res. Atmos.*, *119*, 7833–7841, doi:10.1002/2014JD021471.
Nair, A. S., and J. Indu (2017), Performance assessment of Multi-Source Weighted-Ensemble Precipitation (MSWEP) product over India, *Climate*, *5*(1), 2, doi:10.3390/cli5010002.
Njoku, E. G., T. J. Jackson, V. Lakshmi, T. K. Chan, and S. V. Nghiem (2003), Soil moisture retrieval from AMSR-E, IEEE transactions on geoscience and remote sensing, *41*(2), 215–229, doi:10.1109/TGRS.2002.808243.
Owe, M., R. de Jeu, and T. Holmes (2008), Multisensor historical climatology of satellite-derived global land surface moisture, *J. Geophys. Res.*, *113*, F01002, doi:10.1029/2007JF000769.
Pal, J. S., E. A. Eltahir, and E. E. Small (2000), Simulation of regional-scale water and energy budgets—Representation of subgrid cloud and precipitation processes within RegCM, *J. Geophys. Res.*, *105*, 29,579–29,594, doi:10.1029/2000JD900415.
Paris Anguela, T., M. Zribi, S. Hasenauer, F. Habets, and C. Loumagne (2008), Analysis of surface and root-zone soil moisture dynamics with ERS scatterometer and the hydrometeorological model SAFRAN-ISBA-MODCOU at Grand Morin watershed (France), *Hydrol. Earth Syst. Sci.*, *12*(6), 1415–1424, doi:10.5194/hess-12-1415-2008.
Pearson, K. (1895), Note on regression and inheritance in the case of two parents, *Proc. R. Soc. Lond.*, *58*, 240–242, doi:10.1098/rspl.1895.0041.
Peel, M. C., B. L. Finlayson, and T. A. McMahon (2007), Updated world map of the Köppen-Geiger climate classification, *Hydrol. Earth Syst. Sci. Discuss.*, *4*(2), 439–473, doi:10.5194/hess-11-1633-2007.
Piao, S., et al. (2010), The impacts of climate change on water resources and agriculture in China, *Nature*, *467*(7311), 43–51, doi:10.1038/nature09364.
Priestley, C. H. B., and R. J. Taylor (1972), On the assessment of surface heat flux and evaporation using large scale parameters, *Mon. Weather Rev.*, *100*(81–92), 1972, doi:10.1175/1520-0493(1972)100<0081:OTAOSH>2.3.CO;2.
Prigent, C., F. Aires, and W. B. Rossow (2003), Land surface skin temperatures from a combined analysis of microwave and infrared satellite observations for an all-weather evaluation of the differences between air and skin temperatures, *J. Geophys. Res.*, *108*(D10), 4310, doi:10.1029/2002JD002301.
Qiu, J., Q. Gao, S. Wang, and Z. Su (2016), Comparison of temporal trends from multiple soil moisture data sets and precipitation: The implication of irrigation on regional soil moisture trend, *Int. J. Appl. Earth Obs. Geoinf.*, *48*, 17–27, doi:10.1016/j.jag.2015.11.012.
Rebel, K. T., R. A. M. de Jeu, P. Ciais, N. Viovy, S. L. Piao, G. Kiely, and A. J. Dolman (2012), A global analysis of soil moisture derived from satellite observations and a land surface model, *Hydrol. Earth Syst. Sci.*, *16*, 833–847, doi:10.5194/hess-16-833-2012.
Reichle, R. H., J. V. Ardizzone, G. K. Kim, R. A. Lucchesi, E. B. Smith, and B. H. Weiss (2015), Soil Moisture Active Passive (SMAP) Mission Level 4 Surface and Root Zone Soil Moisture (L4_SM) Product Specification Document, SMAP Project, Global Modeling and Assimilation Office, Goddard Space Flight Center, Greenbelt, MD, USA. GMAO Office Note No. 10 (Version 1.4), 90 pp. [Available at http://nsidc.org/data/docs/daac/smap/sp_l4_sm/pdfs/Reichle789.pdf.]
Renard, B., et al. (2008), Regional methods for trend detection: Assessing field significance and regional consistency, *Water Resour. Res.*, *44*, W08419, doi:10.1029/2007WR006268.
Rodell, M., P. R. Houser, U. E. A. Jambor, and J. Gottschalck (2004), The global land data assimilation system, *Bull. Am. Meteorol. Soc.*, *85*(3), 381, doi:10.1175/BAMS-85-3-381.
Roxy, M. K., K. Ritika, P. Terray, R. Murtugudde, K. Ashok, and B. N. Goswami (2015), Drying of Indian subcontinent by rapid Indian Ocean warming and a weakening land-sea thermal gradient, *Nat. Commun.*, *6*, doi:10.1038/ncomms8423.
Scipal, K., M. Drusch, and W. Wagner (2008), Assimilation of a ERS scatterometer derived soil moisture index in the ECMWF numerical weather prediction system, *Adv. Water Resour.*, *31*(8), 1101–1112, doi:10.1016/j.advwatres.2008.04.013.
Scipal, K., C. Scheffler, and W. Wagner (2005), Soil moisture-runoff relation at the catchment scale as observed with coarse resolution microwave remote sensing, *Hydrol. Earth Syst. Sci. Discuss.*, *2*(2), 417–448, doi:10.5194/hess-9-173-2005.
Sen, P. K. (1968), Robustness of some nonparametric procedures in linear models, *Ann. Math. Stat.*, 1913–1922 http://www.jstor.org/stable/223929.
Seneviratne, S. I., T. Corti, E. L. Davin, M. Hirschi, E. B. Jaeger, I. Lehner, B. Orlowsky, and A. J. Teuling (2010), Investigating soil moisture–climate interactions in a changing climate: A review, *Earth Sci. Rev.*, *99*(3), 125–161, doi:10.1016/j.earscirev.2010.02.004.
Shao, L. (2004), Sand-dust storm, population and environment in northwest China, *Chinese J. Pop. Resour. Environ.*, *2*(4), 17–24, doi:10.1080/10042857.2004.10677384.
Sheffield, J., and E. F. Wood (2008), Global trends and variability in soil moisture and drought characteristics, 1950-2000, from observation-driven simulations of the terrestrial hydrologic cycle, *J. Clim.*, *21*(3), 432–458, doi:10.1175/2007JCLI1822.1.
Shi, W., F. Tao, and J. Liu (2014), Regional temperature change over the Huang-Huai-Hai plain of China: The roles of irrigation versus urbanization, *Int. J. Climatol.*, *34*(4), 1181–1195, doi:10.1002/joc.3755.
Siebert, S., P. Döll, J. Hoogeveen, J. M. Faures, K. Frenken, and S. Feick (2005), Development and validation of the global map of irrigation areas, *Hydrol. Earth Syst. Sci. Discuss.*, *2*(4), 1299–1327, doi:10.5194/hess-9-535-2005.
Simmons, A. J., K. M. Willett, P. D. Jones, P. W. Thorne, and D. P. Dee (2010), Low-frequency variations in surface atmospheric humidity, temperature, and precipitation: Inferences from reanalyses and monthly gridded observational data sets, *J. Geophys. Res.*, *115*, D01110, doi:10.1029/2009JD012442.
Small, E. E., F. Giorgi, and L. C. Sloan (1999), Regional climate model simulation of precipitation in central Asia: Mean and interannual variability, *J. Geophys. Res.*, *104*, 6563–6582, doi:10.1029/98JD02501.

Stern, H., G. de Hoedt, and J. Ernst (2000), Objective classification of Australian climates, *Aust. Meteorol. Mag.*, *49*(2), 87–96.
Su, B., A. Wang, G. Wang, Y. Wang, and T. Jiang (2016), Spatiotemporal variations of soil moisture in the Tarim River basin, China, *Int. J. Appl. Earth Obs. Geoinf.*, *48*, 122–130, doi:10.1016/j.jag.2015.06.012.
Su, C. H., D. Ryu, W. Dorigo, S. Zwieback, A. Gruber, C. Albergel, R. H. Reichle, and W. Wagner (2016), Homogeneity of a global multisatellite soil moisture climate data record, *Geophys. Res. Lett.*, *43*, 11,245–11,252, doi:10.1002/2016GL070458.
Su, Z., J. Wen, L. Dente, R. van der Velde, L. Wang, Y. Ma, K. Yang, and Z. Hu (2011), The Tibetan Plateau observatory of plateau scale soil moisture and soil temperature (Tibet-Obs) for quantifying uncertainties in coarse resolution satellite and model products, *Hydrol. Earth Syst. Sci.*, *15*(7), 2303–2316, doi:10.5194/hess-15-2303-2011.
Szczypta, C., J. C. Calvet, C. Albergel, G. Balsamo, S. Boussetta, D. Carrer, S. Lafont, and C. Meurey (2011), Verification of the new ECMWF ERA-Interim reanalysis over France, *Hydrol. Earth Syst. Sci.*, *15*(2), 647, doi:10.5194/hess-15-647-2011.
Tan, J., C. Jakob, W. B. Rossow, and G. Tselioudis (2015), Increases in tropical rainfall driven by changes in frequency of organized deep convection, *Nature*, *519*(7544), 451–454, doi:10.1038/nature14339.
Tan, L., Y. Cai, Z. An, H. Cheng, C. C. Shen, Y. Gao, and R. L. Edwards (2016), Decreasing monsoon precipitation in southwest China during the last 240 years associated with the warming of tropical ocean, *Clim. Dyn.*, 1–10, doi:10.1007/s00382-016-3171-y.
Taylor, C. M. (2015), Detecting soil moisture impacts on convective initiation in Europe, *Geophys. Res. Lett.*, *42*, 4631–4638, doi:10.1002/2015GL064030.
Taylor, C. M., R. A. de Jeu, F. Guichard, P. P. Harris, and W. A. Dorigo (2012), Afternoon rain more likely over drier soils, *Nature*, *489*(7416), 423–426, doi:10.1038/nature11377.
Tett, S. F., P. A. Stott, M. R. Allen, W. J. Ingram, and J. F. Mitchell (1999), Causes of twentieth-century temperature change near the Earth's surface, *Nature*, *399*(6736), 569–572, doi:10.1038/21164.
Triantafyllou, G. N., and A. A. Tsonis (1994), Assessing the ability of the Köppen system to delineate the general world pattern of climates, *Geophys. Res. Lett.*, *21*, 2809–2812, doi:10.1029/94GL01992 .
Trigo, I. F., S. Boussetta, P. Viterbo, G. Balsamo, A. Beljaars, and I. Sandu (2015), Comparison of model land skin temperature with remotely sensed estimates and assessment of surface-atmosphere coupling, *J. Geophys. Res. Atmos.*, *120*, 12,096–12,111, doi:10.1002/2015JD023812.
Viterbo, P., and A. C. Beljaars (1995), An improved land surface parameterization scheme in the ECMWF model and its validation, *J. Clim.*, *8*(11), 2716–2748, doi:10.1175/1520-0442(1995)008<2716:AILSPS>2.0.CO;2.
Wagner, W., et al. (2013), The ASCAT soil moisture product: A review of its specifications, validation results, and emerging applications, *Meteorol. Z.*, *22*(1), 5–33, doi:10.1127/0941-2948/2013/0399.
Wagner, W., G. Lemoine, and H. Rott (1999), A method for estimating soil moisture from ERS scatterometer and soil data, *Remote Sens. Environ.*, *70*(2), 191–207, doi:10.1016/S0034-4257(99)00036-X.
Wagner, W., V. Naeimi, K. Scipal, R. de Jeu, and J. Martínez-Fernández (2007), Soil moisture from operational meteorological satellites, *Hydrogeol. J.*, *15*(1), 121–131, doi:10.1007/s10040-006-0104-6.
Wang, G., J. Huang, W. Guo, J. Zuo, J. Wang, J. Bi, Z. Huang, and J. Shi (2010), Observation analysis of land-atmosphere interactions over the Loess Plateau of northwest China, *J. Geophys. Res.*, *115*, D00K17, doi:10.1029/2009JD013372.
Wang, G., J. L. Innes, J. Lei, S. Dai, and S. W. Wu (2007), China's forestry reforms, *Science*, *318*(5856), 1556–1557, doi:10.1126/science.1147247.
Yang, B., Y. Zhang, Y. Qian, J. Tang, and D. Liu (2016), Climatic effects of irrigation over the Huang-Huai-Hai Plain in China simulated by the weather research and forecasting model, *J. Geophys. Res. Atmos.*, *121*, 2246–2264, doi:10.1002/2015JD023736.
Yang, J., P. Reichert, K. C. Abbaspour, and H. Yang (2007), Hydrological modelling of the Chaohe Basin in China: Statistical model formulation and Bayesian inference, *J. Hydrol.*, *340*(3), 167–182, doi:10.1016/j.jhydrol.2007.04.006.
Yang, J., P. Reichert, K. C. Abbaspour, J. Xia, and H. Yang (2008), Comparing uncertainty analysis techniques for a SWAT application to the Chaohe Basin in China, *J. Hydrol.*, *358*(1), 1–23, doi:10.1016/j.jhydrol.2008.05.012.
Yang, Y., R. J. Donohue, and T. R. McVicar (2016), Global estimation of effective plant rooting depth: Implications for hydrological modeling, *Water Resour. Res.*, *52*, 8260–8276, doi:10.1002/2016WR019392.
Zhang, D., et al. (2006), Seasonal dynamics of soil CO_2 effluxes with responses to environmental factors in lower subtropical forests of China, *Sci. China Ser. Earth Sci.*, *49*(2), 139–149, doi:10.1007/s11430-006-8139-z.
Zhang, Y., et al. (2016), Multi-decadal trends in global terrestrial evapotranspiration and its components, *Sci. Rep.*, *6*, doi:10.1038/srep19124.
Zhu, C., and D. P. Lettenmaier (2007), Long-term climate and derived surface hydrology and energy flux data for Mexico: 1925–2004, *J. Clim.*, *20*(9), 1936–1946, doi:10.1175/JCLI4086.1.